

ADVANCED MATERIALS

Supporting Information

for *Adv. Mater.*, DOI: 10.1002/adma.201905288

Coordination Polymer to Atomically Thin, Holey,
Metal-Oxide Nanosheets for Tuning Band Alignment

Sajjad S. Mofarah, Esmail Adabifiroozjaei,* Raheleh Pardehkhorrām, M. Hussein N. Assadi, Manuel Hinterstein, Yin Yao, Xinhong Liu, Mohammad B. Ghasemian, Kourosh Kalantar-Zadeh, Rashid Mehmood, Claudio Cazorla, Reza Shahmiri, Ghazaleh Bahmanrokh, Saroj Bhattacharyya, Maria Chiara Spadaro, Jordi Arbiol, Sean Lim, Yuwen Xu, Hamidreza Arandiyān, Jason Scott, Pramod Koshy,* and Charles C. Sorrell*

Supporting Information

**Coordination Polymer to Atomically-Thin, Holey, Metal-Oxide Nanosheets for Tuning
Band Alignment**

*Sajjad S. Mofarah**, *Esmail Adabifiroozjaei**, *Raheleh Pardehkhorrani*, *M. Hussein N. Assadi*, *M. Hinterstein*, *Yin Yao*, *Xinhong Liu*, *Mohammad B. Ghasemian*, *Kourosh Kalantar-Zadeh*, *Rashid Mahmood*, *Claudio Cazorla*, *Reza Shahmiri*, *Ghazaleh Bahmanrokh*, *Saroj Bhattacharyya*, *Maria Chiara Spadaro*, *Jordi Arbiol*, *Sean Lim*, *Yuwen Xu*, *Hamidreza Arandiyan*, *Jason Scott*, *Pramod Koshy**, and *Charles C. Sorrell*

Table of Contents

Notes	Titles	Page
1	Methods and characterisations	3
2	Ce-CP electrodeposition setup and formation mechanism	13
3	Structural, morphological, and chemical characterisations of Ce-CP	17
4	Characterisation of Ce-CP nanosheets and transformation into CeO _{2-x}	36
5	Characterisation of Ti-CP, Zr-CP and derived holey metal oxide nanosheets	43
6	Tailoring thickness and pore size of the MOs nanosheets	56
7	Characterisation of CeO _{2-x} based TMO heterojunction structures	61
8	Photocatalytic activities of CeO _{2-x} based TMO heterojunction structures	66
9	References	71

1. Methods and characterisations

Synthesis of CPs

Synthesis of Ce-CP

The synthesis of Ce-CP tubes was carried out by chronopotentiometry electrodeposition using an electrochemical station (Ezstat Pro, Indiana, USA, with a resolution of 300 μV and 3 nA (in the $\pm 100 \mu\text{A}$ range) with an undivided three-electrode configuration system.^[1] Fluorine-doped tin oxide on glass (FTO; Wuhan Geo Scientific Education Instrument, China; 3.0 cm \times 1.5 cm; film resistivity $\sim 16 \Omega \text{ sq}^{-2}$), platinum wire (Basi Inc., Indiana, USA, L = 23 cm, D = 0.5 mm), and Ag/AgCl (Basi Inc., Indiana, USA) were used as the working, counter, and reference electrodes, respectively. The electrolyte was prepared from a mixture of 0.05 M glacial trichloroacetic acid (TCA) and 0.05 M $\text{Ce}(\text{NO}_3)_3 \cdot 6\text{H}_2\text{O}$. The initial pH was adjusted using 1 M NaOH solution to 5.8. Prior to electrodeposition, each substrate was cleaned stepwise by ultrasonication in ethanol and acetone for 5 min, followed by activation by immersion (1 cm) in 45% nitric acid for 2 min and drying with compressed nitrogen. Chronopotentiometry electrodeposition at an applied voltage of 1.4V was used to deposit the Ce-CP tubes.

Synthesis of Ti-CP

Ti-CP was prepared by injecting an ice-cold solution of TiCl_4 (27.41 μL , 0.25 mmol) into a mixture of DMF (4 mL) and formic acid (7.5 mL) followed by heating at 100°C for 16 h. The as-synthesized powder was subsequently washed with DMF and acetone *via* three cycles of centrifugation (5000 g, 20 min) and the obtained Ti-CP powder was dried at 60°C for 24 h under vacuum.

Synthesis of Zr-CP

In an identical synthesis procedure to Ti-CP, Zr-CP was synthesized following the protocol reported in the literature.^[2] In a typical procedure, ZrCl₄ (58 mg, 0.25 mmol) was added to a mixture of dimethylformamide (DMF; 4 mL) and formic acid (7.5 mL) followed by sonication at room temperature for 10 min. The obtained clear solution was then transferred into a Teflon-lined stainless steel vessel and was heated at 100°C for 16 h. After cooling to room temperature, the resultant white powder was washed three times with DMF (5000 g, 20 min) and then solvent-exchanged with acetone. The final product was dried at 60°C for 24 h under vacuum to remove the solvents.

Synthesis of MCP and MO nanosheets

1. CeO_{2-x} nanosheet: The Ce-CP powder (50 mg) was added to 50 mL of DI water (pH ~ 7) and then stirred (100 rpm) for 5 min followed by ultrasonication at room temperature for 10 min. Then, 10 ml NaOH solution (3 M) was added dropwise, resulting in the transformation of the Ce-CP into CeO_{2-x}. The resultant nanosheets were collected and washed with water (DI). The final product was then air-dried at 100°C for 24 h. This approach yielded nanosheets as thin as 1.1 nm.

2. Large-scale CeO_{2-x} nanosheet: 700 mg of Ce-CP was added to 200 mL of DI water at room temperature followed by stirring for 72 h using a magnetic stirrer (100 rpm). Large sheets with a width of up to 0.5 cm were produced in this way (Figure S28). These large-scale sheets were basically formed from stacking of atomic-scale thin nanosheets that were formed in DI water. Longer times usually resulted in the synthesis of wider and thicker sheets. Addition of NaOH (3 M) converted the Ce-CP to CeO_{2-x}. Next, the dispersion phase was filtered using a filter paper to separate the CeO_{2-x} sheets from the liquid. The resultant sheets were dried at 100°C for 12 h in an oven. This approach resulted in large-scale production of CeO_{2-x} nanosheets by a very simple, quick and efficient method.

3. TiO₂ nanosheet: TiO₂ nanosheets were prepared by adding 10 mg of Ti-CP powder into 5 mL of DI water followed by stirring (500 rpm) at room temperature for 3 h. Then, 5 mL of NaOH (0.1 M) solution was added to the mixture, and the stirring was continued at room temperature for 2 h. The obtained turbid mixture was washed three times with DI water (10000 g, 20 min) and the resulting nanosheets were dried at 60°C for 24 h.

4. ZrO₂ nanosheet: ZrO₂ nanosheets were prepared by adding 10 mg of the Zr-CP powder into 5 mL of DI water followed by stirring (500 rpm) at room temperature for 3 h. Then, 5 mL of NaOH (0.1 M) solution was added to the mixture, and the stirring was continued at room temperature for 2 h. The obtained turbid mixture was washed three times with DI water (10000 g, 20 min) and the resulting nanosheets were dried at 60°C for 24 h.

Synthesis of MCP and MO nanosheets

FCO: The Ce-CP nanosheets were first prepared by adding 24 mg of Ce-CP powder into 15 mL of DI water followed stirring (100 rpm) at room temperature and adding NaOH dropwise with magnetic stirring over ~10-30 min, until the pH reached 8, as monitored by a pH metre, to obtain CeO₂ holey nanosheets. This is followed by dispersion of CeO₂ nanosheet in an aqueous solution with the pH of 6 (decreasing the pH by dropping HCl). This was done in accordance with the information in the Fe Pourbaix diagram [Figure S50], which showed that this pH was suitable for the purpose of initiating oxidation of dissolved Fe²⁺ to form precipitated Fe₂O₃. Then, 5 mL of iron (II) chloride (FeCl₂) solution (0.3 mM) was added to the acidic Ce-CP nanosheet solution (pH = 6) followed by addition of 2 mL of NaOH (1 M) under gentle stirring which was continued for 30 min. The resultant turbid mixture was washed with DI water (10000 g, 40 min) and heated at 200°C for 24 h.

1. NCO: The Ce-CP nanosheets were first prepared by adding 24 mg of Ce-CP powder into 15 mL of DI water followed by increasing pH to 8 and stirring (100 rpm) at room temperature for 15 min. Then, 5 mL of nickel (III) nitrate (Ni(NO₃)₂•6H₂O) aqueous solution

(0.3 mM) was added to the acidic Ce-CP nanosheet solution (pH = 6) followed by addition of 2 mL of NaOH (1M) under gentle stirring which was continued for 30 min. The resultant turbid mixture was washed with DI water (10000 g, 40 min) and heated at 200°C for 24 h.

2. ZCO: The Ce-CP nanosheets were first prepared by adding 24 mg of Ce-CP powder into 15 mL of DI water followed by increasing pH to 8 and stirring (100 rpm) at room temperature for 15 min. Then, 5 mL of zinc (II) nitrate ($\text{Zn}(\text{NO}_3)_2 \cdot 6\text{H}_2\text{O}$) aqueous solution (0.3 mM) was added to the acidic Ce-CP nanosheet solution (pH = 6) followed by addition of 2 mL of NaOH (1 M) under gentle stirring continued for 30 min. The resultant turbid mixture was washed with DI water (10000 g, 40 min) and heated at 200°C for 24 h.

Characterisation

Transmission electron microscopy (TEM)

Dry powder of the specimens was suspended in water and drop-cast onto a carbon-supported Cu grid followed by air-drying at room temperature. The prepared samples were used for TEM, scanning transmission electron microscopy (STEM), high angle annular dark-field (HAADF), energy dispersive spectroscopy (EDS), and electron energy loss spectroscopy (EELS) analysis. High-resolution transmission TEM (HRTEM) images and EDS analysis of the nanostructures were taken by a Philips CM 200 microscope (Eindhoven, the Netherlands), while HAADF images, and EELS analysis were conducted by JEOL JEM-ARM200F microscope (Tokyo, Japan). Both machines were operated at an accelerating voltage of 200 kV. Additionally, the beam flux was reduced to very low values of ~ 15 pA to minimize the beam damage effects. Finally, spectroscopy was conducted using spectrum imaging mode with sub-pixel scanning operative. This procedure ensured that at all times during the acquisition, the beam was moving, and the local fluence was minimized. Also, to avoid the beam damage on the sample during EELS measurement, the sample was cooled down to liquid nitrogen temperature.

Scanning electron microscopy (SEM)

Scanning electron microscopy images were obtained by SEM (FEI Nova NanoSEM; secondary electron emission; accelerating voltage 5 kV, Hillsboro, OR, USA).

X-ray photoelectron spectroscopy (XPS)

Surface analysis of the samples was carried out using a Thermo Fisher Scientific ESCALAB 250Xi spectrometer (Loughborough, Leicestershire, UK) equipped with a monochromatic Al K α source (1486.6 eV) hemispherical analyzer. The XPS samples were prepared by drop-casting an aqueous suspension of the nanostructure on the substrates followed by air-drying at room temperature. The pressure in the analysis chamber was maintained < 8-10 mbar during the acquisition of the XPS data. All binding energies are referenced to the C1s signal corrected to 285 eV and the spectra were fitted using a convolution of Lorentzian and Gaussian profiles.

X-ray diffraction (XRD)

Mineralogical data for the nanostructures were obtained using a Philips X'Pert Multipurpose X-ray diffractometer (Almelo, Netherlands) with CuK α radiation of [0.15405 nm], 2θ of 20°-80°, step size of 0.02°, and scanning speed of 5.5° 2θ min⁻¹. The peaks were analyzed using X'Pert High Score Plus software (Malvern, UK).

Neutron diffraction (ND)

Neutron diffraction patterns for structural analysis were collected on the high-intensity powder diffractometer Wombat, installed on the Open Pool Australian Light-water (OPAL) reactor at the Australian Nuclear Science and Technology Organisation (ANSTO). Two datasets with 1.63 Å and 2.41 Å were collected based on a CaAlNaF₃ standard sample.

Raman spectroscopy (Raman)

Raman data were collected using a Renishaw inVia confocal Raman microscope (Gloucestershire, UK) equipped with a helium-neon green laser (514 nm) and diffraction grating of 1800 g mm^{-1} . All Raman data were recorded at laser power of 35 mW and a spot size of $\sim 1.5 \text{ }\mu\text{m}$. The data analysis was performed using Renishaw WiRE 4.4 software and the spectra were calibrated with respect to the silicon peak located at $\sim 520 \text{ cm}^{-1}$.

Thermogravimetric analysis (TGA)

The decompositions of the Ce-CPs were assessed by using thermogravimetric analysis (TGA; TA Instruments, Q5000, $20^\circ\text{--}1000^\circ\text{C}$, $10^\circ\text{C min}^{-1}$ heating rate at different atmospheres of nitrogen and air.

Fourier transform infrared spectroscopy (FTIR)

ATR-FTIR; Spotlight 400 FTIR, PerkinElmer (Waltham, MA, USA) within the wavelength of $400\text{--}4000 \text{ cm}^{-1}$ was used to determine the chemical species present in the Ce-CP.

Ab-initio molecular dynamics (MD) simulation

Density functional calculations were performed based on augmented plane wave pseudopotentials^[3] with Perdew-Burke-Ernzerhof functional^[4] as implemented in the VASP code.^[5] For the electronic setting, a fine Monkhorst-Pack k-point grid with a spacing of 0.05 \AA^{-1} and an energy cut-off of 520 eV were used. To find the ground state configuration, we ran a quenching *ab initio* molecular dynamics simulations was run based on a micro-canonical ensemble with a target temperature of 20 K with steps of 0.1 fs for 10 ps. Full geometry optimization was then carried out on the equilibrated structure, with convergence criteria for

the energy and forces of 10^{-6} eV and 10^{-2} eV \AA^{-1} , respectively. The final geometry optimization run was conducted with Van der Waals correction (vdw-DFT) based on Michaelides's approach applied.^[6]

Atomic force microscopy (AFM)

The thickness of nanosheets was measured by atomic force microscopy (AFM; Bruker Dimension Icon SPM, PeakForce Tapping mode). A ScanAsyst-Air probe (Bruker AFM probes) was installed in the AFM holder and used for all measurements. The samples were printed on either glass or silicon substrate by applying a slight vacuum. The pixel resolution was 512 samples/line. A slow scan rate of 0.195 Hz was used to ensure accuracy. The peak force was minimized to avoid sample deformation and the feedback gain settings were optimized accordingly. The thicknesses of the thin films were determined using height profile with line and box scanning.

Kelvin probe force microscopy (KPFM)

Amplitude modulated KPFM (AM-KPFM) measurement were performed using the Bruker Dimension ICON SPM with a Nanoscope V controller. A platinum-iridium coated AFM tip (SCM-PIT-V2, Bruker AFM probes) was used to scan the surface. The probe was firstly installed on a cantilever holder, and the laser was aligned onto the back of the cantilever. Then the probe was tuned near its resonance frequency with a small offset to the right hand side of the resonance curve (typically for normal tapping mode image, we tune to the left side of the resonance curve, which makes the interaction force on the surface slightly repulsive. However, it was found for KPFM measurements, the offset to the right-hand side provided better results in selected specimens). The oscillation amplitude was kept around 30 to 40 nm, depending on the specimen. The amplitude setpoint and gains were adjusted accordingly for each specimen.

The scan rate was around 0.3 to 0.4 Hz with a scan size of 10 μms and 512 samples per line as the resolution. The scan setting included: Amplitude setpoint = 172 mV, gains = 1.1, scan rate = 0.326 Hz. Further, the operating parameters were as follows: The lift height was fixed at 50 nm for the specimens to avoid any influence from surface topography (sometimes a smaller lift height of 30 nm is used when scanning smaller areas). The drive2 amplitude of the AC bias applied to the tip during the lift pass was set to 500 mV with a 170° phase angle. Also, for calibration tests, which were done before and after measuring the specimen, the same AFM tip was also measured against a freshly cleaved HOPG sample and/or a pre-calibrated TiO_2 on a silicon reference sample. This calibration was important to determine the work function of the platinum tip, which can vary significantly from tip to tip.

Photoluminescence (PL) spectroscopy

PL was done using a spectrofluorophotometer (RF-5301PC, Shimadzu, Kyoto, Japan). The samples were used as free-standing stacked nanosheets.

Zetapotential measurement

The zeta potential also was determined using Zetasizer Nano ZS (Malvern Instruments, 4 mW He-Ne laser, 633 nm). For this work, the CeO_{2-x} and heterojunction nanostructures were suspended in 3 mL of deionized water at a concentration of $20 \mu\text{g mL}^{-1}$ using 10 mL individual glass tubes. The suspensions were sonicated for 2 min prior to running the measurement.

First-principles calculations details

First-principles calculations based on density functional theory (DFT)^[7] are performed to simulate and analyze the band structure differences between ceria nanosheets, the corresponding bulk system, and 0D/2D heterostructures. We use the PBEsol functional^[8] as

implemented in the VASP software.^[9] A “Hubbard-U” scheme^[10] with $U = 3$ eV is employed for a better treatment of the localized Ce $4f$, Fe $3d$, Ni $3d$, and Zn $3d$ electronic orbitals. We use the “projector augmented wave” method to represent the ionic cores^[11] by considering the following electrons as valence: Ce $4f$, $5d$, $6s$, and $4d$; Fe $3d$ and $4s$; Ni $3d$ and $4s$; Zn $3d$ and $4s$; and O $2s$ and $2p$. Wave functions are represented in a plane-wave basis truncated at 650 eV. For integrations within the Brillouin zone we employ Monkhorst-Pack k-point grids with a density equivalent to that of $16 \times 16 \times 16$ in the fluorite CeO₂ unit cell. Geometry relaxations are performed with a conjugate-gradient algorithm that allows for simulation cell shape and volume variations. The relaxations are halted when the forces in the atoms fall all below $0.01 \text{ eV} \cdot \text{\AA}^{-1}$. By using these technical parameters we obtain zero-temperature energies that are converged to within 0.5 meV per formula unit. In order to estimate accurate electronic densities of states and band gaps, we employ the hybrid HSE06 exchange-correlation functional^[12] to perform single-point calculations on the equilibrium geometries determined at the PBEsol+U level.

Ceria nanosheets were simulated as two-unit cells thick CeO₂ slabs oriented along the $\{111\}$ direction. The pristine surface of such slab systems are non-polar, which is convenient from a simulation point of view. Determination of the energetically most favourable transition metal adsorption sites was performed by analyzing all possible positions on the surface of the nanosheet. For all the considered species, we found that the preferred transition metal adsorption site was on top of the circumcentre of the triangle formed by three neighbouring oxygen atoms in the surface of the nanosheet. Transition metal adsorption energies were calculated with the formula $E_{\text{ads}} = E_{\text{TM@2DCO}} - E_{\text{2DCO}} - E_{\text{TM}}$, where the different terms represent the zero-temperature energy of the TM@2DCO heterostructure, ceria nanosheet (2DCO), and isolated transition metal ion (TM). The amount of charge transferred from the transition metal ions to the ceria nanosheet upon adsorption was calculated by performing the

Bardeen analysis.^[13] The content of transition metal ions in the DFT simulations was of 6% as referred to the number of cerium atoms.

Photocatalytic activity test

The photocatalytic activity of the nanostructures was evaluated for degradation of methylene blue (MB, M9140, dye content ≥ 82 wt%, Sigma-Aldrich) in aqueous solution under solar irradiation^[14]. In the presence of the nanosheets, the gradual decrease in the intensity of MB absorbance peak at 664 nm was recorded by using a UV-Visible spectrometer (UV-Vis, PerkinElmer Lambda 35, aperture 20 mm \times 10 mm). The concentration of the nanosheet samples was set to 0.5 mg/mL in 50 mL of MB solution with a concentration of 1×10^{-5} M. The suspension was illuminated by 100 mW cm⁻² irradiance power under simulated 1 sun AM 1.5 light, for 0-120 min at 20 min intervals. Before irradiation, the suspensions were vigorously stirred with the nanosheets for 20 min in dark condition to eliminate the role of adsorption-desorption-equilibrium between the dyes and the surface of nanosheets during light irradiation. The optical absorption was measured within the range of 400-800 nm after isolating the CeO_{2-x} and heterojunction nanostructures (10000 g, 10 min) from the solution. The high photocatalytic stability of the heterojunctions nanostructure was tested by the use of the same samples for repeating the photodegradation tests.

2. Ce-CP electrodeposition setup and formation mechanism

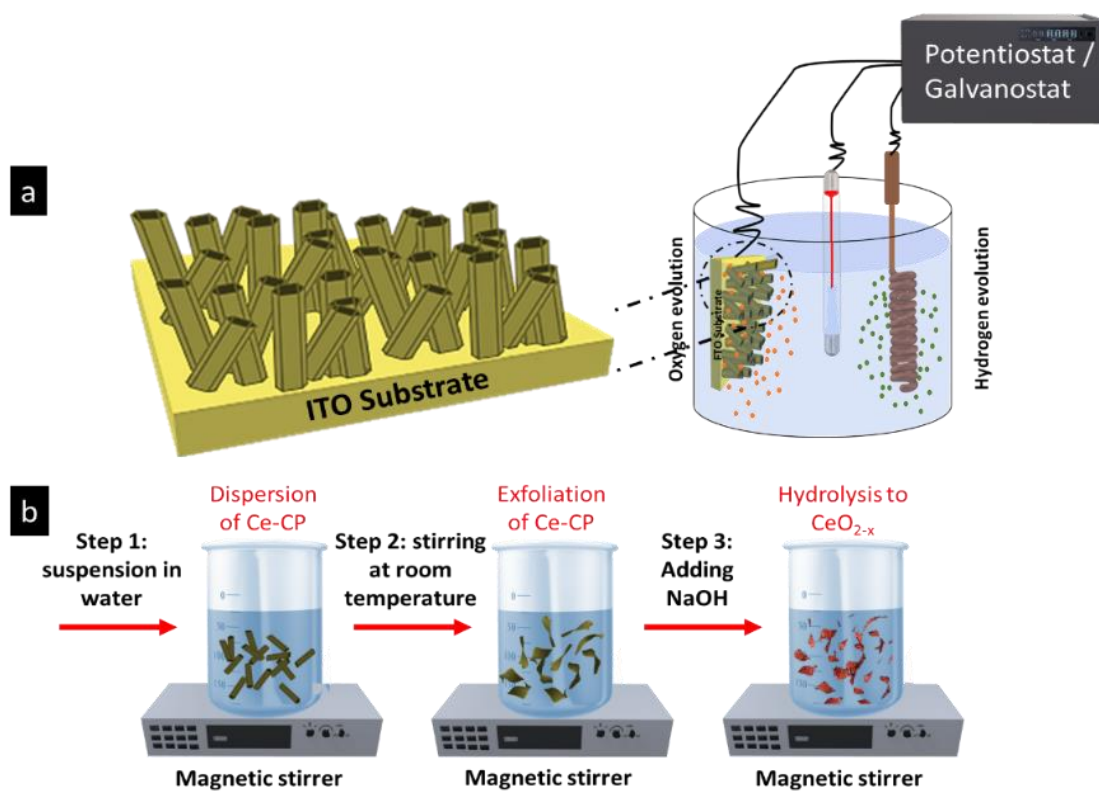


Figure S1. Schematic illustration of a) Three-electrode electrochemical cell used for the synthesis of Ce-CP tubes under vigorous oxygen evolution and deposition of free-standing hexagonal tubes of Ce-CP on fluorine-doped tin oxide (FTO) substrate. b) CeO_{2-x} formation through the three-step process including exfoliation of the Ce-CP tubes into Ce-CP nanosheets and subsequently oxidation of Ce-CP nanosheet into holey CeO_{2-x} nanosheet.

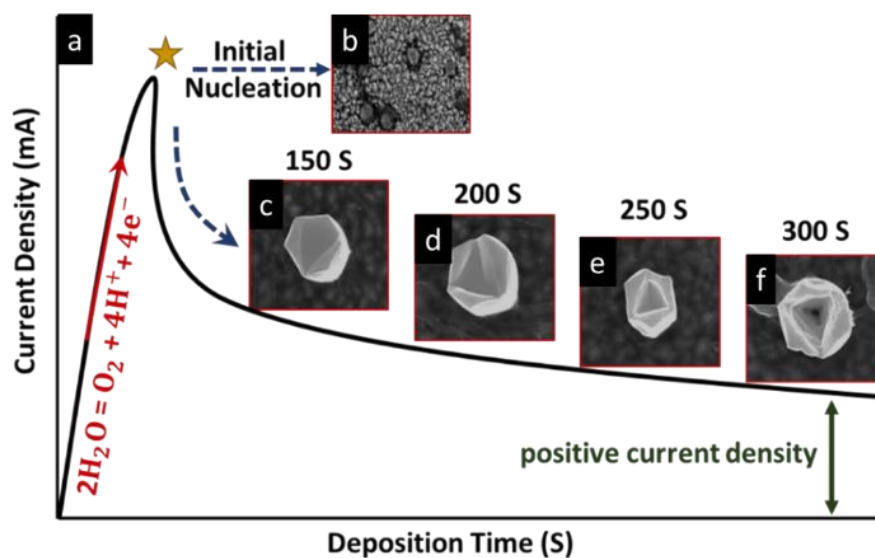


Figure S2. Formation mechanism of Ce-CP tubes under constant current electrochemical deposition. a) current-deposition time plot; b-f) SEM images representing the nucleation/growth process of the Ce-CPs tube as a function of electrodeposition time.

Electrodeposition of the Ce-CP was carried out by using chronoamperometry technique, in which the current varies as a function of deposition time, while a constant potential is applied. Figure S2 shows current-deposition time plot, where the current density increases rapidly for the initial stages of the deposition. The high current density is attributed to the oxygen evolution reaction at the working electrode (FTO substrate). However, the current density drops after ~ 100 s of applying a potential followed by a gradual decrease after ~ 160 s. The variations in current density was studied by analysis nucleation/growth mechanism using SEM imaging, as a function of deposition times (inset of Figure S2). The image obtained at the peak current density (Figure S2b) revealed small nuclei of the Ce-CP. The low-conductivity of the Ce-CP polymer, compared to the FTO substrate is likely to result in a drop in the current density. The continued growth of the Ce-CP polymer led to a decrease in the exposed FTO surface and thus, reduction of the current density. Interestingly, Figure S2c shows that nuclei are grown

vertically against the substrate while forming a hexagonal rod after 150 s of deposition. Increase in the deposition time (Figure S2d) resulted in the formation of a hole at the centre of the hexagonal rod and finally, the transition of the hexagonal rod to the hexagonal tube (Figure S2f). This transition can be attributed to the effect of the application of high current density, which resulted in the travel of generated oxygen bubbles perpendicular to the substrate. Therefore, the evolution of morphology moves towards minimization of the Ce-CP contact surface with the FTO substrate, owing to enhance the accessibility of water at the FTO substrate leading to subsequent oxygen evolution reactions.

Thermodynamic analyses of Ce(III) and Ce(IV) in Ce^{3+} - Ce^{4+} - CCl_3COOH - H_2O system

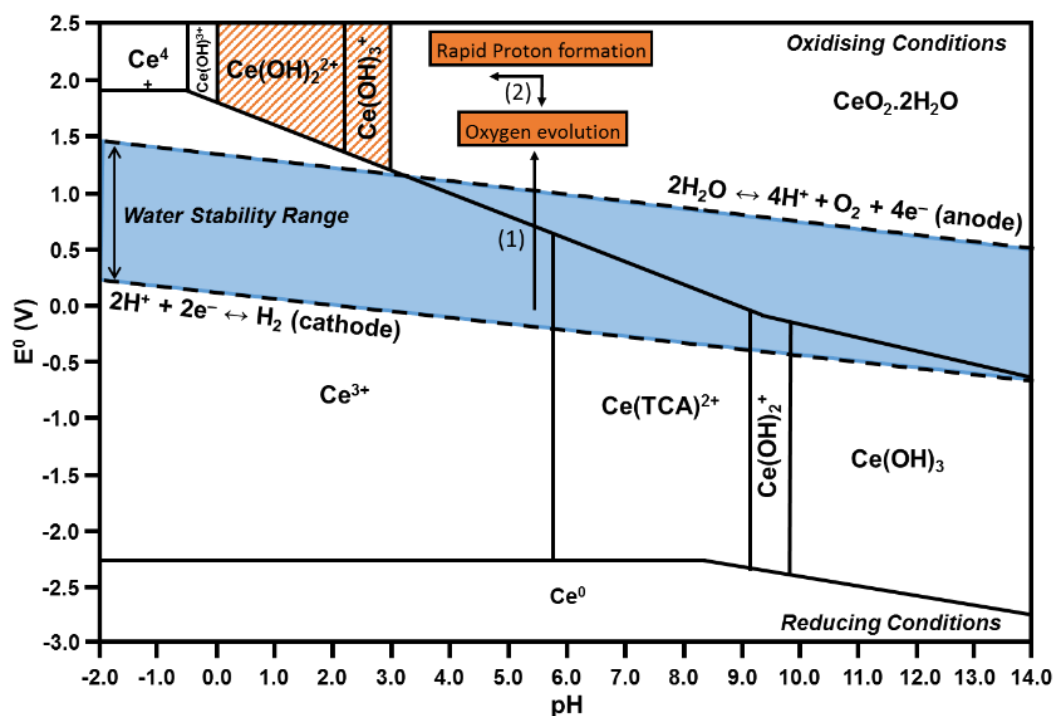


Figure S3. Thermodynamic study on the quarterly aqueous system Ce(III)-Ce(IV)-TCA- H_2O as a function of pH

Applying high current density in the oxygen evolution region resulted in a high production rate of oxygen bubbles at the region adjacent to the FTO substrate. The high O_2 concentration environment results in an oxidation of Ce(III) species to Ce(IV), which is shown as the step (1)

in Figure S3. From the other side, according to water splitting reaction, the evolution of one mole oxygen is followed by the formation of 4 moles of protons that lead to a rapid drop in the local pH and hence the formation of a highly acidic atmosphere. All these reactions occur above the water stability range labelled blue in Figure S3.

From previous reports, the stability regions of Ce(IV) species in aqueous solution exist due to the high field strength (affinity to hybridization) of Ce(IV) species^[15]. Therefore the oxidation of Ce(III) species to Ce(IV), even under acidic pH, results in the formation of Ce(IV) hydroxide but with unsaturated coordination bonds. This is also shown in the Pourbaix diagram (Figure S3), where the formation of Ce(IV) hydroxide with low coordination number occurs followed by the rapid proton generation (step(2)). In the final step, the presence of TCA molecules with unstable Ce(IV) species leads to coordination bonding between the Ce(IV) hydroxide and TCA linker, forming a monolayer structure. The existence of high concentration of protons, owing to the acidic pH, is very critical since the protons intercalate at the interlayer spaces of Ce(IV) and TCA coordinated monolayer structure and establish Van der Waals interactions between the layers resulting in the formation of $(\text{Ce}(\text{OH})_2(\text{TCA})_2 \cdot 2\text{H}_2\text{O})$.

3. Structural, morphological, and chemical characterisations of Ce-CP

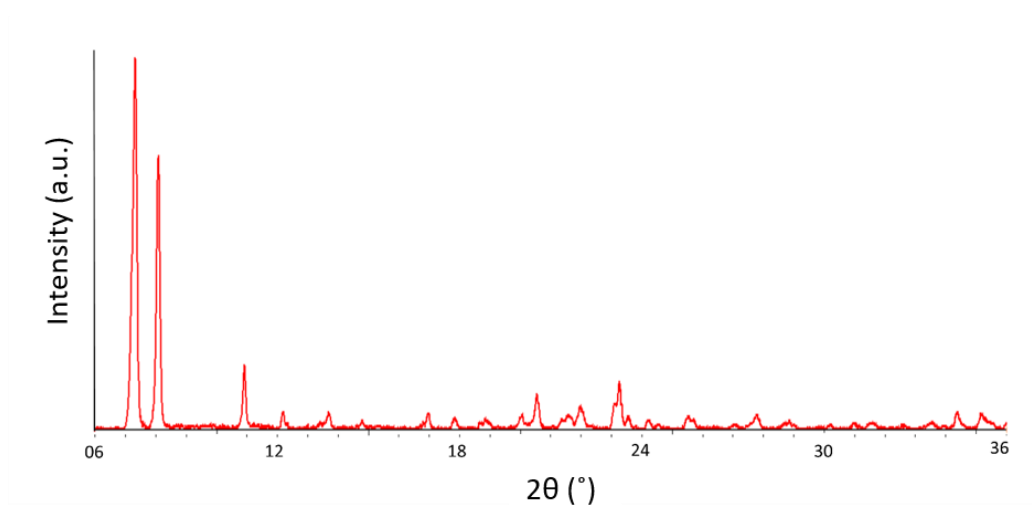


Figure S4. Experimental X-ray pattern of Ce-CP.

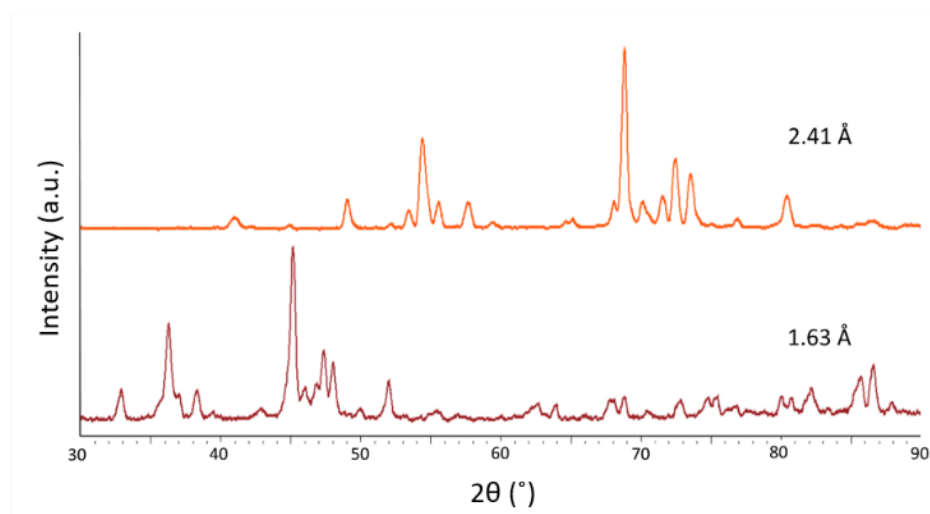


Figure S5. Neutron diffraction pattern of Ce-CP obtained at wavelengths of 1.63 Å and 2.41 Å.

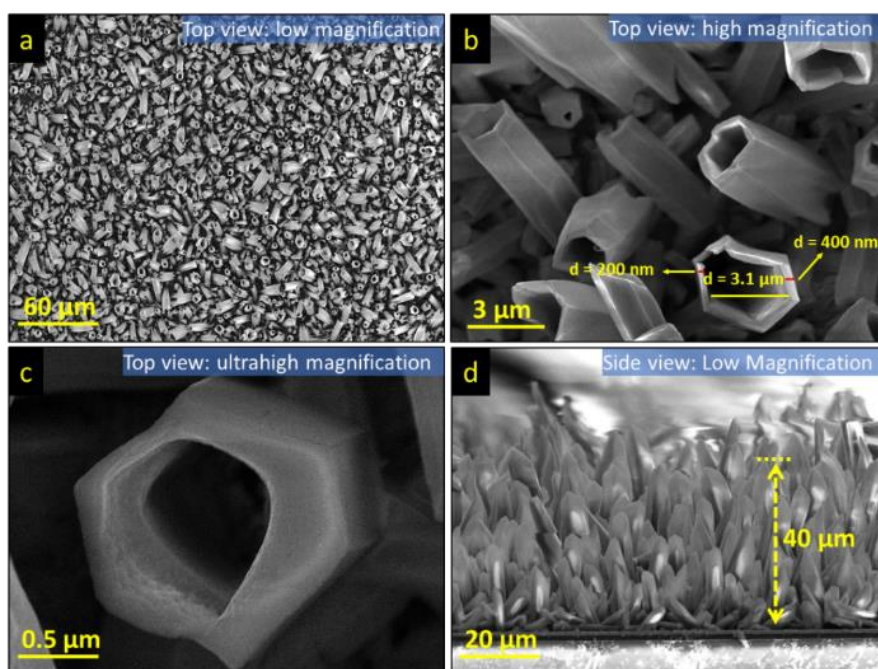


Figure S6. SEM images of Ce-CP tubes grown on FTO substrate.

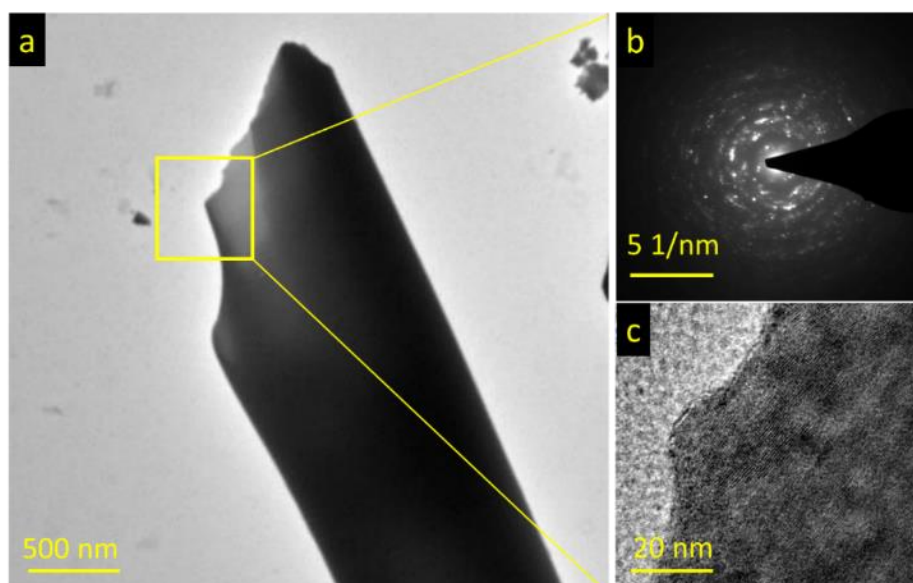


Figure S7. a) The low magnification TEM image of a single Ce-CP tube. b) selected area electron diffraction pattern of region shown in the yellow box and c) HRTEM image of region shown in the red box.

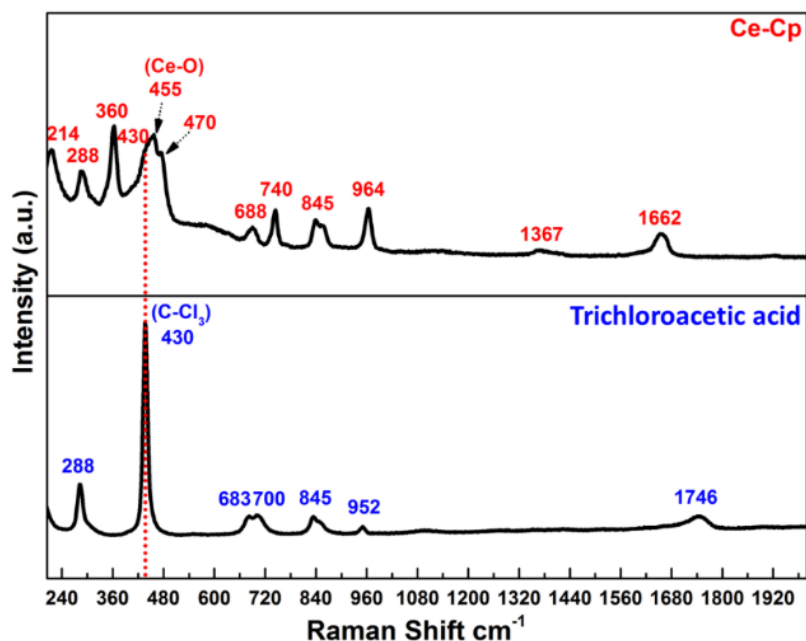


Figure S8. Raman spectra of Ce-CP tube (top) and trichloroacetic acid (bottom).

Description of Raman data: The Raman spectra of the Ce-CP was analysed comprehensively and indexed according to the vibrational modes of pure TCA, as explained below:

A brief look at the data indicates that some of the peaks observed in Ce-CP spectra are also present in TCA spectra, indicating the existence of TCA molecule in the Ce-CP. The peaks centred at 288 and 430 cm^{-1} are attributed to the asymmetric and symmetric bending vibrations of the C-Cl bond, respectively^[16]. Additionally, the peak at 688 cm^{-1} belongs to symmetric stretching vibration mode of C-Cl bond, while peaks at 845 and 744 cm^{-1} are due to asymmetric stretching vibration mode of the same bond^[17]. The peak positioned at 952 cm^{-1} corresponds to the symmetric vibration mode of the carbon-carbon bond (C-C)^[16]. Further comparison of the two spectra shows that Raman shifts occurred in some of the peaks (952 cm^{-1} to 962 cm^{-1} , 700 cm^{-1} to 740 cm^{-1} , and 683 cm^{-1} to 688 cm^{-1}), which are attributed to the alteration in vibrational modes of the bonds in TCA structure due to interaction with cerium ions^[18]. Additionally, in TCA, there is a peak at 1746 cm^{-1} corresponding to the vibrational mode of the free carboxylic group (COO), which is split into two peaks at 1367 (symmetric stretching

vibration) and 1662 cm^{-1} (asymmetric stretching vibration) in Ce-CP spectra^[18]). The splitting seems likely due to the interactions between the COO group and Ce that results in the formation of Ce-O bond, the peak of which appears at 455 cm^{-1} . The peaks at 214 cm^{-1} and 360 cm^{-1} are correlated to in- and out-of-phase vibration modes of the Ce-CP structure. There are two dominant peaks positioned at 455 and 470 cm^{-1} in Ce-CP spectra. The former is ascribed to the symmetric stretching vibration of cerium and its coordinated oxygen^[19], while the latter originates from the vibration mode of cerium bonded with chlorine and oxygen.

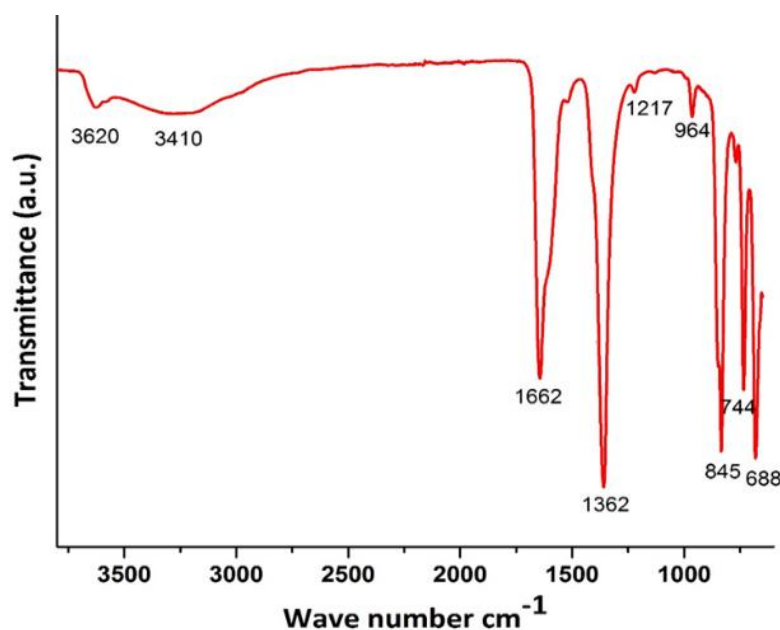


Figure S9. FTIR spectra of Ce-CP tubes.

Description of FTIR data: The bands centred at 3620 and 3410 cm^{-1} show stretching vibration of hydroxyl groups revealing the presence of water and OH group in the Ce-CP^[18]. The peaks at 1660 and 1360 cm^{-1} are attributed to the asymmetric and symmetric stretching mode of a carboxylic group that is bonded to cerium cations. Also, the peaks at 1040 cm^{-1} and 966 cm^{-1} are due to the bending vibration of the carboxylic group and symmetric vibration mode of the

carbon-carbon bond (C-C), respectively^[20]. Similar to Raman spectra, the peaks at 688, 744, and 845 cm^{-1} are attributed to C-Cl vibration modes.

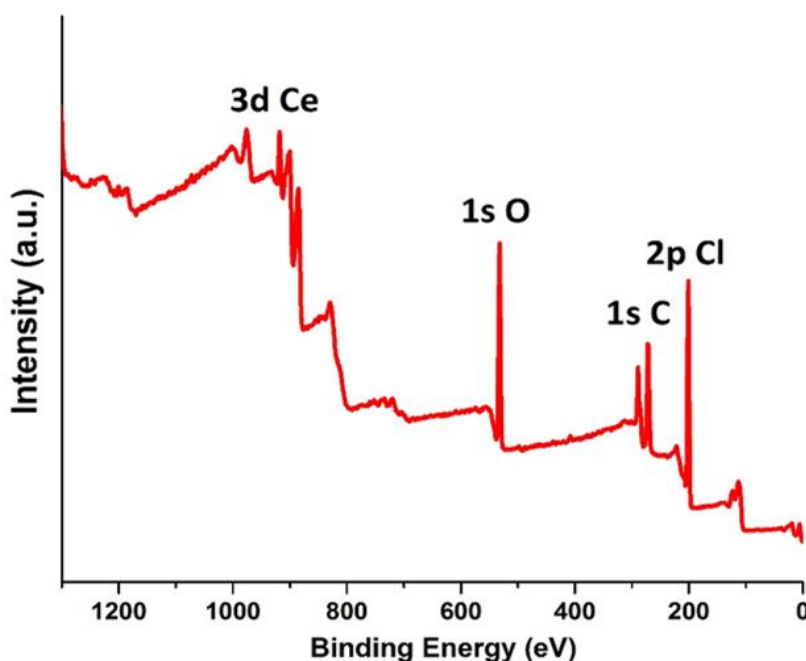


Figure S10. XPS data of Ce-CP tubes.

Description of XPS data: The peaks corresponding to $3d$, $1s$, $1s$, and $2p$ orbitals of cerium, oxygen, carbon, and chlorine elements can be detected at binding energies ranging from 880-920, 529-535, 284-292, and 198-202 eV, respectively. For the cerium, there are two oxidation states of Ce^{3+} and Ce^{4+} representing a spin-orbit combination of electrons in the d-orbital ($3d_{5/2}$ and $3d_{3/2}$). The corresponding binding energies of Ce^{4+} and Ce^{3+} in $3d_{5/2}$ configuration are located at 883, 889, and 899 and 881, and 886 eV, respectively (Table S1). The peak positioned at 530 eV corresponds to hydroxyl bonded to Ce^{4+} .^[21] The peak of organic oxygen in TCA can be observed at 532 eV. At the binding energy of 534 eV, there is a small broad peak representing structural H_2O ^[21]. All the peak positions are provided in Table S1.

Table S1. Binding energies of different chemical bonds in Ce-CP and TCA.

Element	Chemical State	Peak Position Binding Energy (eV)
Ce	Ce ⁴⁺ -O	883, 889, 899
	Ce ³⁺ -O	881, 886
O	OH- Ce ⁴⁺	530
	O in TCA	532
	O (H ₂ O)	534
Cl	Cl in TCA	200, 202
	Cl-Ce ³⁺	198
C	C-TCA	289

The quantitative analysis of the elements in the Ce-CP structure was carried out by deconvolution of the peaks using Gaussian fitting, the results of which are given in Table S2. From the analysis, the stoichiometry of the Ce-CP is identified, based on atomic percentages to be Ce(OH)_{1.8}(TCA)_{2.0}(H₂O)_{1.0}. Further, the XPS results were used for TGA analysis confirming the molar ratio of the Ce-CP structure from wt%, which is elaborated in the following section.

Table S2. Contribution of different elements in Ce-CP with the stoichiometry based on atomic and weight percentages.

Element	XPS	General		Calculated XPS
	Atomic Contribution (at%)	Molecular Weight (g mol ⁻¹)	MW/Avogadro's Number	Weight Contribution (wt%)
Ce	5.1	140	714	23.0
	1.8		256	8.2
O	9.2	16	147	4.7
	20.9		334	10.7
	4.2		67	2.1
Cl	30.4	35	1066	34.2
	6.4		224	7.2
C	21.9	14	307	9.9
Total	100	-	3115	100

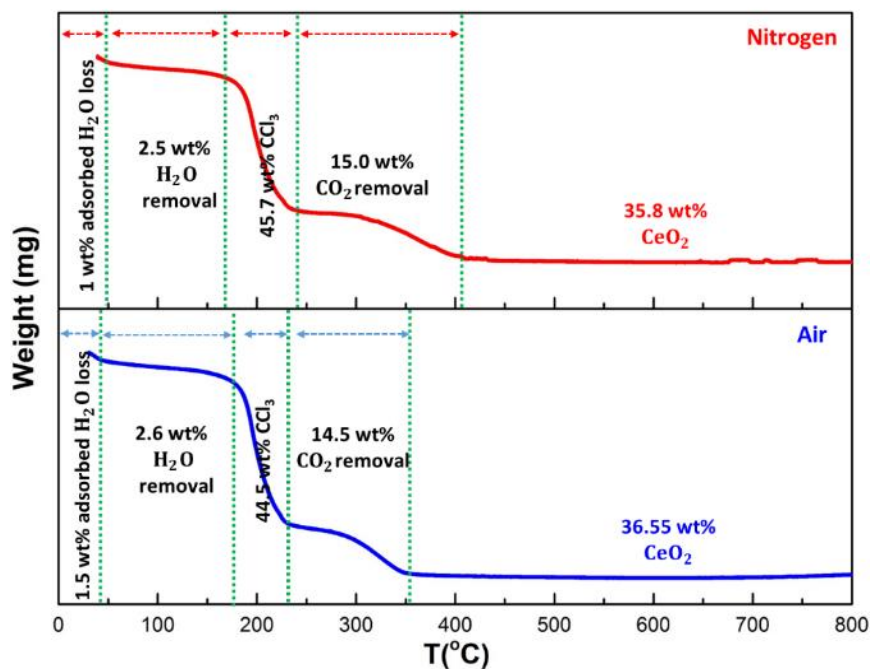


Figure S11. TGA analysis of Ce-CP in nitrogen (top) and air (bottom) atmospheres.

Description of TGA data: TGA analysis of Ce-CP showed similar patterns under both nitrogen and air atmospheres. There are four steps during each of which adsorbed water, structural water, carbon chloride, and CO₂ is removed from the Ce-CP, respectively. The results show that 35.8 wt% of the total Ce-CP is converted to CeO₂ in both conditions. The weight percent of each organic component and the resultant product are given in Table S3, with associated XPS analysis data for comparison. The Ce-CP samples after TGA test were examined by XRD and Raman spectroscopy (not shown here), revealing that heat treatment in both gases results in the formation of CeO₂ cubic fluorite structure.

Table S3. TGA analysis of Ce-CP in air and nitrogen and the associated XPS data.

Elements	TGA (N ₂)		XPS	Difference (%)
	Removal Temperature (°C)	Weight Loss (wt%)	Calculated based on XPS data	
CeO ₂	N/A	35.8	35.9	0.2

	H₂O	160	2.5	2.1	19.0
TCA	CCl₃ in TCA	230	45.7	46.3	-1.3
	CO₂	350	15.0	15.7	4.6

Characterization data of Ce-CP crystal structure: To identify the Ce-CP structure, which does not match with the existing structures in the crystallographic database (The Cambridge Crystallographic Data Centre (CCDC)), we tried to produce Ce-CP single crystals through vapour and layer diffusion methods. However, all attempts resulted in the formation of polycrystalline Ce-CP. Therefore, based on the obtained chemical composition of $(\text{Ce}(\text{OH})_2(\text{TCA})_2 \cdot 2\text{H}_2\text{O})$, and achieved X-ray (1) and neutron (2) diffraction patterns, a Rietveld refinement (using program package FullProf^[22]) was performed, combining all three datasets in order to increase the level of information. The lattice parameters, atomic positions and zero shift parameters were refined. A good fit was obtained for both X-ray and neutron diffraction patterns of Ce-CP (Figure S12 and S13). However, the interpretation of the obtained structure from a physical point of view was challenging due to the uncertainty in the location of lighter elements especially H (Figure S14), while the positions of Ce atoms as well as the lattice parameters were found to be very close to that of experimental data. The structural information of the fitted structure is given in Table S4.

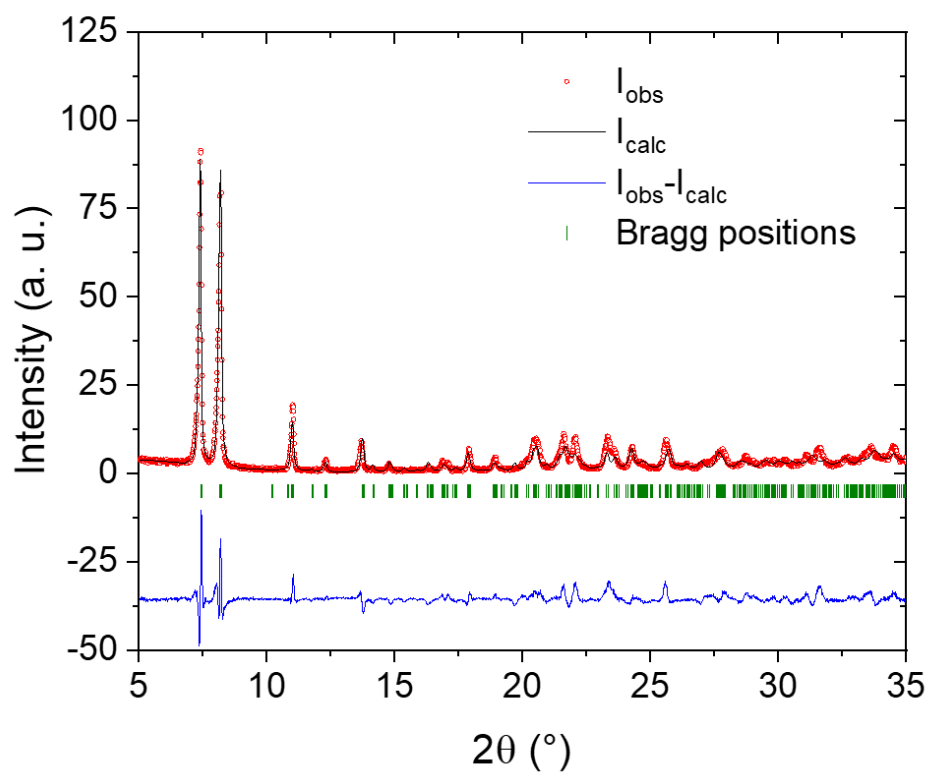


Figure S12. Rietveld-refined X-ray diffraction pattern of Ce-CP.

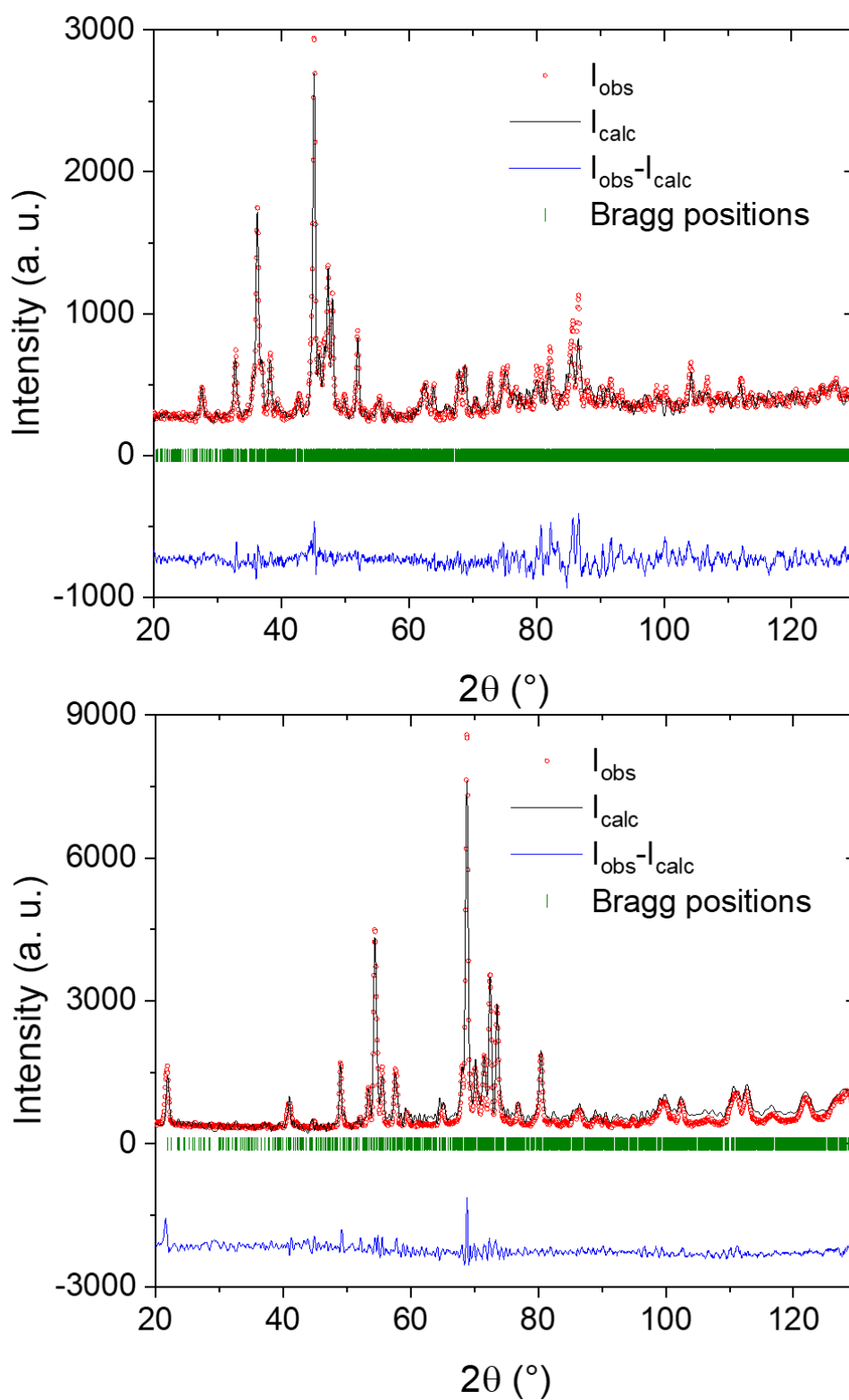


Figure S13. Rietveld-refined neutron diffraction patterns of Ce-CP at wavelength of 1.63 Å (bottom) and 2.41 Å (top).

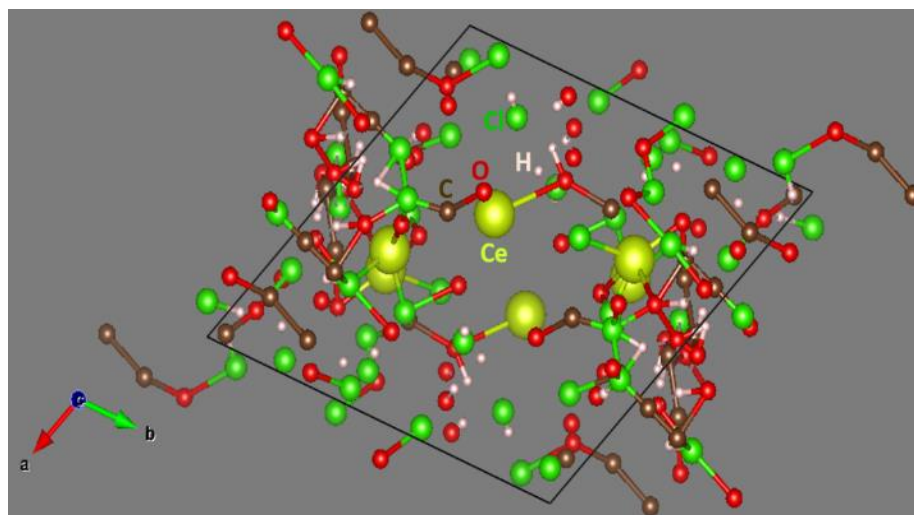


Figure S14. Schematic of refined structure from XRD and ND data.

Table S4.

Crystal data obtained from Rietveld refinement of XRD and ND data

symmetry_cell_setting	Triclinic
symmetry_space_group_name_H-M	'P -1'
symmetry_space_group_name_Hall	'-P 1'

cell_length_a	13.0836(14)
cell_length_b	13.1843(15)
cell_length_c	11.0715(13)
cell_angle_alpha	81.195(7)
cell_angle_beta	93.210(7)
cell_angle_gamma	112.932(6)
cell_volume	1738.1(3)

Atomic coordinates and displacement parameters

loop_

_atom_site_label

_atom_site_fract_x

_atom_site_fract_y

_atom_site_fract_z

_atom_site_U_iso_or_equiv

_atom_site_occupancy

_atom_site_adp_type

_atom_site_type_symbol'

Ce1	0.6005	0.2265	0.6716
Ce2	0.6505	0.2525	0.2096
Ce3	0.4025	0.3805	0.8046
O1	0.6599	0.0548	0.8549
O2	0.3959	0.5709	0.48610
O3	0.6379	0.6819	-0.09710
O4	0.46510	0.7389	0.59110
O5	0.2069	0.09510	0.86810
O6	0.49910	1.04610	0.86413
O7	0.0529	0.32712	0.94613
O8	0.2099	0.8278	0.37910
O9	0.2969	0.09110	0.16110
O10	0.8379	0.94210	0.09410
O11	0.4319	-0.1309	0.98111
O12	0.7529	0.5329	0.27110
O13	0.3589	0.1159	0.55510
O14	0.2169	0.6289	0.15110
O15	0.5299	0.2069	-0.12410
O16	0.8829	0.6068	0.58711
O17	0.1869	0.44510	-0.10210
O18	0.0869	0.5729	0.95411
O19	0.0339	0.7249	0.23011
O20	0.7879	0.21710	0.22510
O21	0.7858	0.0549	0.24310
O22	0.4879	-0.02210	0.87612
O23	0.6239	-0.1068	0.23310
O24	0.1149	0.94510	0.46310
C1	0.8397	1.0609	0.9979
C2	0.0289	0.9678	0.3969

C11	0.8245	0.3306	0.0256
C12	0.2736	0.4625	0.1936
C13	0.9005	0.3925	0.3506
C14	0.0425	0.6155	0.3736
C15	0.9675	0.2015	0.3396
C16	0.0305	0.3986	0.1577
C3	0.5399	0.99410	0.24810
C4	0.8798	0.9547	0.3779
C11	0.53011	0.9879	0.3039
C12	0.8968	0.2137	0.0038
C14	0.9195	0.9385	0.8006
C15	0.1576	0.2576	0.6977
C16	0.2456	0.9425	0.5536
C5	0.2909	0.8518	0.9789
C6	0.6298	0.9178	0.6629
C17	0.4416	-0.0495	0.5146
C18	0.7245	0.3655	0.5286
C19	0.2776	0.7986	0.1506
C116	0.6406	-0.0725	0.0606
C117	0.5026	0.7955	0.7555
C118	0.4655	0.1746	1.0026
C7	0.6618	0.1148	0.2989
C8	0.3269	0.9639	-0.0539
C9	0.7397	0.3887	0.2789
C10	0.4488	0.2788	-0.0069
C110	0.2726	0.1515	0.3786
C111	0.9635	0.8885	0.0466
C112	0.6386	0.4035	0.0466
H1	0.91415	0.67917	1.04200
H2	0.85114	0.37413	0.53916
H3	0.81217	0.61516	0.25416
H4	0.60414	0.07413	0.97717
H5	0.90715	1.02413	0.70519
H6	0.02815	-0.03814	-0.00617
H7	0.84514	0.60113	0.76117
H8	0.49613	0.98516	0.60818
H9	0.57514	0.98816	0.13017
H10	0.29813	0.47713	0.02415
H11	0.11713	0.21114	0.75416
H12	0.89314	0.13514	0.46314
H13	0.09315	0.67414	0.76214
H14	0.25514	0.39615	0.62116
H15	0.39615	-0.01815	0.64817
H16	0.54215	0.91814	1.00018
H17	0.73515	0.14515	0.92117
H18	0.68913	0.92014	-0.01318

In order to obtain a physically meaningful structure, the refined lattice by the Rietveld method was used as a guideline (particularly the lattice parameters and Ce position) for density functional theory and subsequent *ab initio* molecular dynamics calculations. To draw an approximate picture of the coordination environment around cerium atom in the Ce-CP structure, we first used a small stoichiometric supercell comprising of $\text{Ce}(\text{OH})_2(\text{TCA})_2 \cdot 2\text{H}_2\text{O}$ with a sixth of the volume of the refined experimental structure (Figure S14). We exhaustively compared many coordination possibilities such as Ce being coordinated with TCA's Cl and O atoms. The relaxed structure of the most stable coordination is shown in Figure S15. We found that Ce was coordinated by seven O atoms; two from the OH group, two from each of the water molecules, and three from the two TCA molecules. We then used the geometry obtained in Figure S14 to fill the six distinct lattice points of the experimentally refined $\text{P}\bar{1}$ structure. To find the ground state configuration of a larger supercell, we ran quenching *ab initio* molecular dynamics simulations based on a micro-canonical ensemble with a target temperature of 20 K with steps of 0.1 fs for 10 ps. The molecular dynamics simulation was effective in finding a reasonable initial structure for geometry optimization.^[23] Full geometry optimization was then carried out on the equilibrated structure, with convergence criteria for the energy and forces of 10^{-6} eV and 10^{-2} eV \AA^{-1} , respectively. The final geometry optimization included the Van der Waals correction (vdw-DFT) based on Michaelides's approach.^[6] The schematic of the structure is given in Figure S16, while its structural information is given in Table S5. To analyse the coordination environment of the Ce atoms in the large supercell, we calculated the crystal orbital overlap population (COOP) using LOBSTER code.^[24] We identified the bonds connected to Ce atoms by counting all pairs with positive integrated COOP with Ce at one end. Positive integrated COOP values demonstrate that bonding orbitals between Ce and ligands were occupied. We found that all such bonds were formed between Ce and O. Each Ce atom was found to have bonds with eight neighbouring O atoms at an average bond length of 2.61

Å. Six of the Ce-O bonds were found to be rather weak judged by large bond lengths approaching ~ 3 Å and meagre integrated COOP values at an average of 0.05. Some of these bonds may break at room temperature due to thermal fluctuations. As a result, the average coordination number of Ce atom at room temperature is predicted to be between seven and eight, matching exactly the XPS and TGA results shown in Figure S10 and 11. Figure S17 compares the low angle peaks of the X-ray diffraction pattern of experimental Ce-CP, Rietveld refined structure and *ab initio* molecular dynamics simulated structure. As seen, the final optimized structure reproduces the main diffraction peaks at low angles centered at 7.34982° and 8.13390° with reasonable accuracy. It should be noted that the low resolution of the XRD measurement limits the use of the experimental diffraction pattern for evaluating the DFT optimized structures. Consequently, comparison with the measured pattern can only evaluate the position of larger atoms, whereas finer details such as the H-bond network and the position of hydrogens can barely be assessed based on this comparison.^[24a, 25]

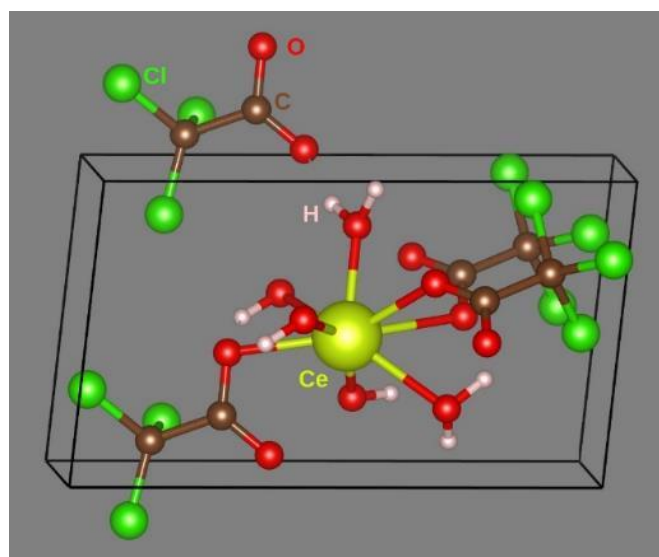


Figure S15. The relaxed structure of the smallest possible Ce-CP unit cell used as the building block for constructing a more realistic structure model.

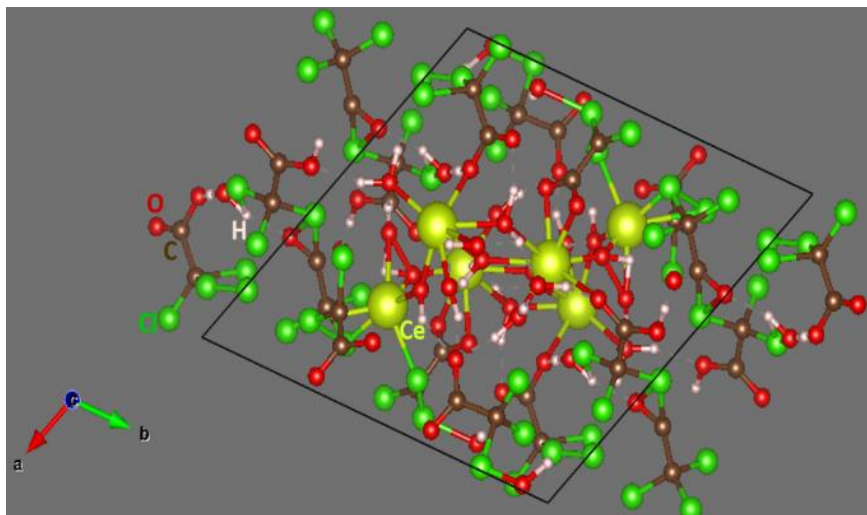


Figure S16. The final relaxed structure of Ce-CP unit cell.

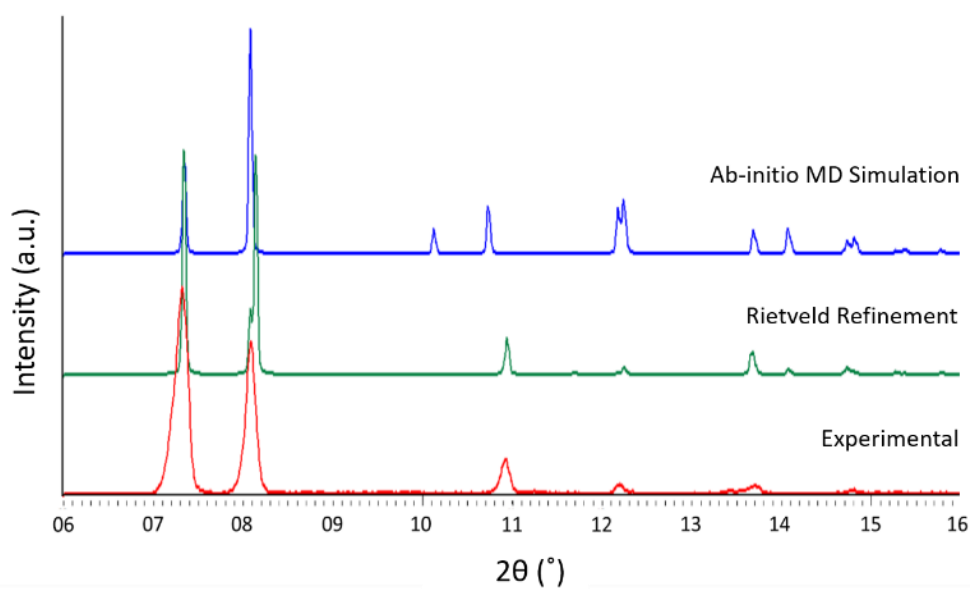


Figure S17. Comparison of X-ray patterns of experimental, Rietveld refined, and ab initio MD simulated structures.

Table S5.

Crystal data obtained from ab initio geometry optimization

symmetry_cell_setting	Triclinic
-----------------------	-----------

symmetry_space_group_name_H-M	'P -1'
symmetry_space_group_name_Hall	'-P 1'

cell_length_a	13.0836(14)
cell_length_b	13.1843(15)
cell_length_c	11.0715(13)
cell_angle_alpha	81.195(7)
cell_angle_beta	93.210(7)
cell_angle_gamma	112.932(6)
cell_volume	1738.1(3)

Atomic coordinates and displacement parameters

loop_

_atom_site_label

_atom_site_type_symbol

_atom_site_fract_x

_atom_site_fract_y

_atom_site_fract_z

_atom_site_U_iso_or_equiv

_atom_site_adp_type

_atom_site_occupancy

O1	0.56104	0.88831	0.24802
O2	0.22733	0.44109	0.19882
O3	0.64398	0.79267	0.49433
O4	0.52245	0.25412	0.20137
O5	0.62572	0.32240	0.45520

O6	0.64889	0.13287	0.03088
O7	0.48504	0.56295	0.37019
O8	0.48783	0.40246	0.04051
O9	0.79574	0.71277	0.16151
O10	0.94129	0.74983	0.42943
O11	0.59301	0.58006	0.13985
O12	0.03896	0.36760	0.15570
O13	0.39470	0.38803	0.23527
O14	0.38673	0.58204	0.05332
O15	0.34907	0.63559	0.27008
O16	0.67349	0.00429	0.42884
O17	0.51241	0.07717	0.18452
O18	0.44554	0.80003	0.49203
O19	0.03622	0.69683	0.14770
O20	0.68090	0.74596	0.28420
O21	0.17619	0.64251	0.10461
O22	0.01357	0.08421	0.03480
O23	0.71450	0.46388	0.23253
O24	0.72107	0.55807	0.39056
H1	0.66349	0.76596	0.42071
H2	0.09140	0.07044	0.02118
H3	0.64664	0.25935	0.49469
H4	0.52982	0.94727	0.23439
H5	0.64354	0.92812	0.25518
H6	0.67072	0.87574	0.47617
H7	0.50181	0.84612	0.42812
H8	0.41920	0.39112	0.14440
H9	0.32180	0.39939	0.23204
H10	0.67852	0.61889	0.14122
H11	0.51505	0.34352	0.08042
H12	0.56691	0.51773	0.08602
H13	0.41206	0.56055	0.32834
H14	0.28340	0.58024	0.23471
H15	0.57348	0.10152	0.10782
H16	0.32929	0.51146	0.09421
H17	0.91941	0.74661	0.51579
H18	0.46191	0.56702	0.45611
Ce1	0.55253	0.41600	0.35071
Ce2	0.51433	0.71388	0.15791
Ce3	0.27651	0.67594	0.43731
Cl1	0.40344	-0.01663	0.42049
Cl2	0.38147	0.18970	0.41215
Cl3	0.89228	0.16224	0.32820
Cl4	0.24655	0.27451	0.05182
Cl5	0.27398	0.05108	0.21744
Cl6	0.00933	0.20030	0.06443
Cl7	0.72974	0.25334	0.25829
Cl8	0.85760	0.30502	0.48123

C9	0.13342	0.17083	0.28827
C10	0.87841	0.92084	0.39704
C11	0.99305	0.89950	0.19823
C12	0.79974	0.97355	0.15359
C13	0.15636	0.80914	0.36132
C14	0.33714	0.85235	0.19063
C15	0.15772	0.99037	0.49594
C16	0.94154	0.59542	0.45704
C17	0.13841	0.48364	0.41706
C18	0.93847	0.48024	0.24626
C1	0.79325	0.20187	0.38330
C2	0.48363	0.14888	0.23000
C3	0.38693	0.09307	0.32146
C4	0.77763	0.76910	0.23442
C5	0.13477	0.36618	0.16898
C6	0.14127	0.25734	0.14999
C7	0.86826	0.88131	0.25539
C8	0.69833	0.10136	0.45379
C9	0.13382	0.69980	0.16174
C10	0.20942	0.76346	0.25001
C11	0.76885	0.51835	0.32038
C12	0.88200	0.52918	0.34364

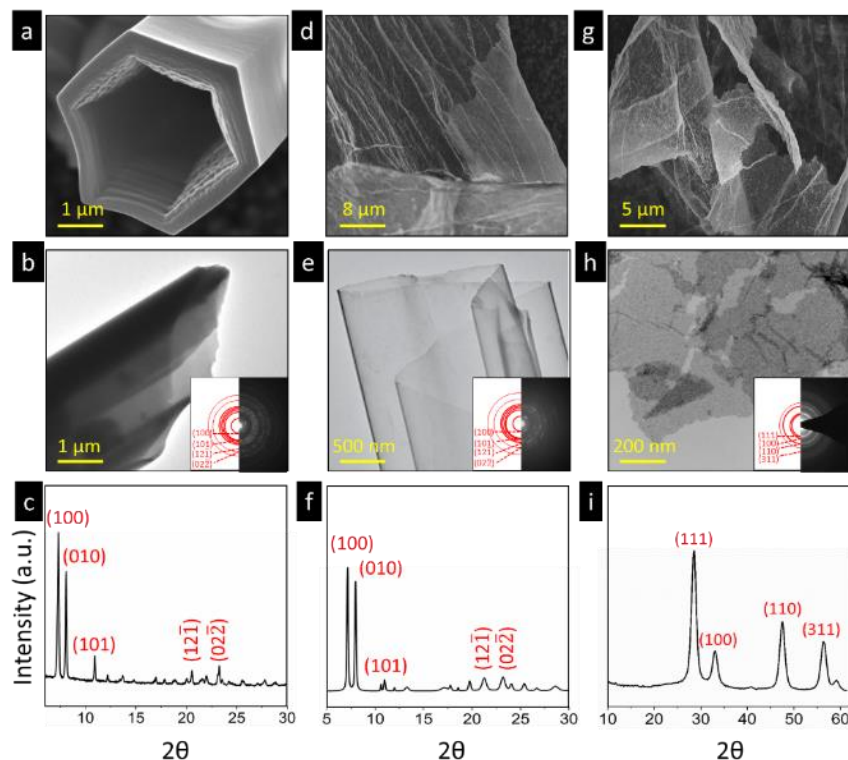
4. Characterisation of Ce-CP nanosheets and transformation into CeO_{2-x} 

Figure S18. Structural and morphological evolution of Ce-CP hexagonal nanotube into CeO_{2-x} nanosheets. a) SEM image of Ce-CP hexagonal nanotube. b) TEM image of Ce-CP hexagonal nanotube (inset: SAED pattern). c) XRD pattern of Ce-CP hexagonal nanotube. d) SEM image of Ce-CP nanosheet. e) TEM image of Ce-CP nanosheet (inset: SAED pattern). f) XRD pattern of Ce-CP nanosheet. g) SEM image of holey CeO_{2-x} nanosheet. h) TEM image of holey CeO_{2-x} nanosheet (inset: SAED pattern). i) XRD pattern of CeO_{2-x} nanosheet.

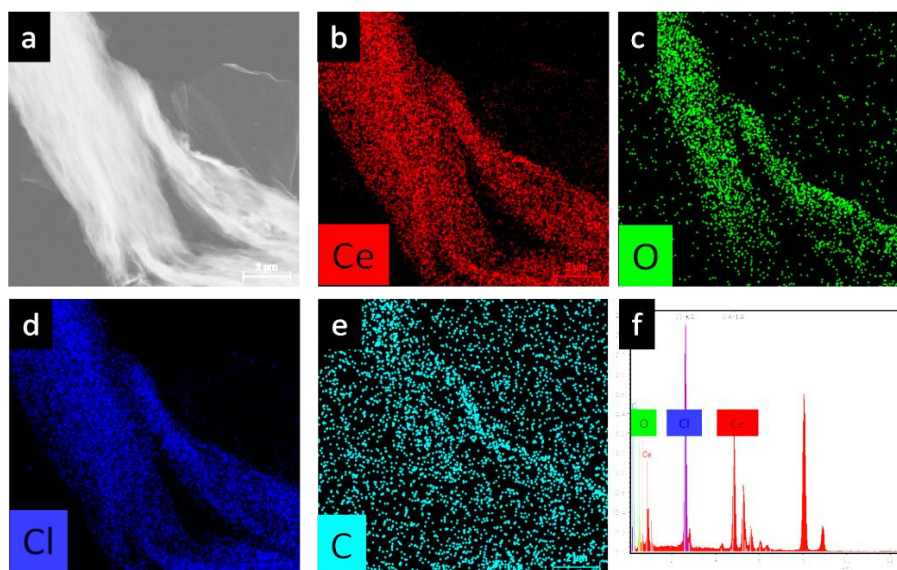


Figure S19. a) TEM image of Ce-CP nanosheet. EDS elemental mapping image of b) cerium (red), c) oxygen (green), d) chlorine (navy blue), e) carbon (light blue). f) EDS spectra of Ce-CP nanosheet.

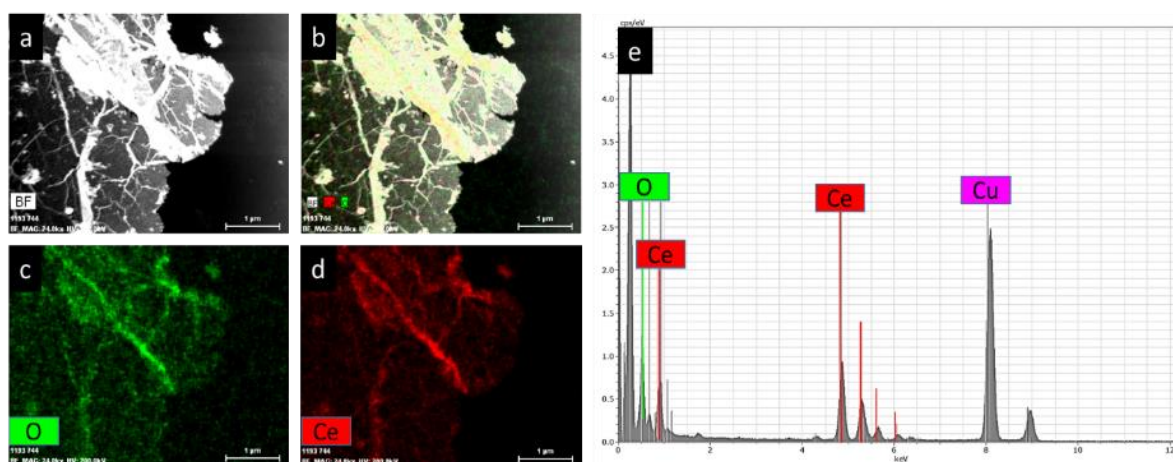


Figure S20. a,b) The bright field TEM image of CeO_{2-x} holey nanosheets. EDS elemental mapping image of c) oxygen (green), d) cerium (red). e) EDS spectra of CeO_{2-x} holey nanosheets.

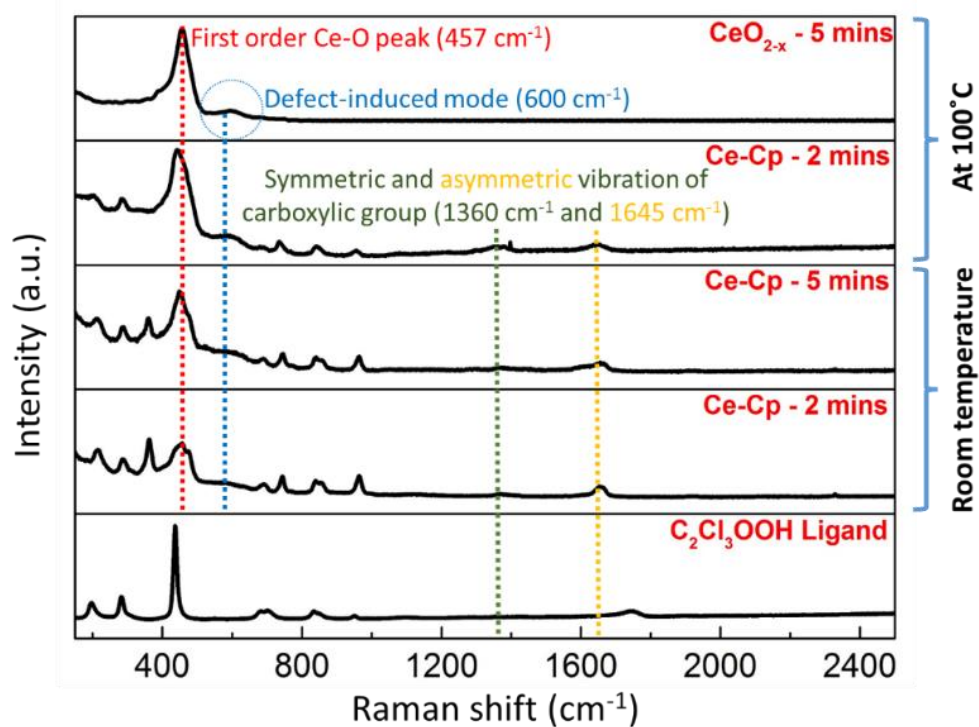


Figure S21. Raman of CeO_{2-x} nanosheets compared with that of original Ce-CP, indicating insignificant differences.

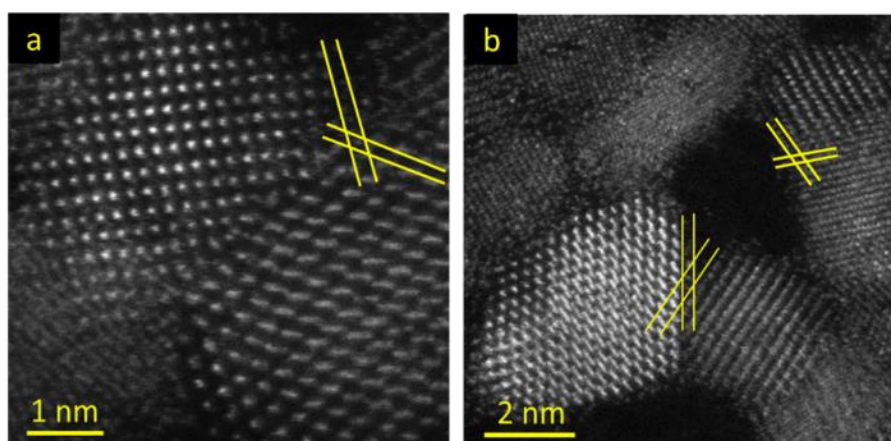


Figure S22. HAADF images of holey CeO_{2-x} nanostructure illustrating intergrowth of crystallites.

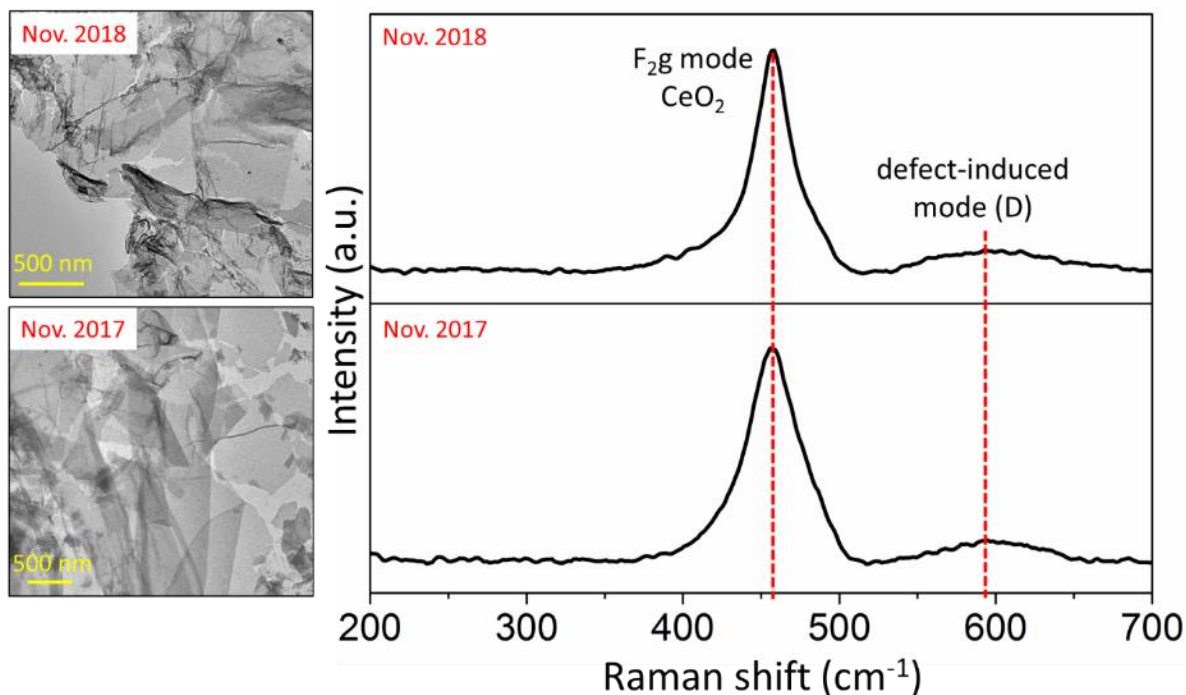


Figure S23. Confirmation of CeO_{2-x} nanosheet stability after 1 year.

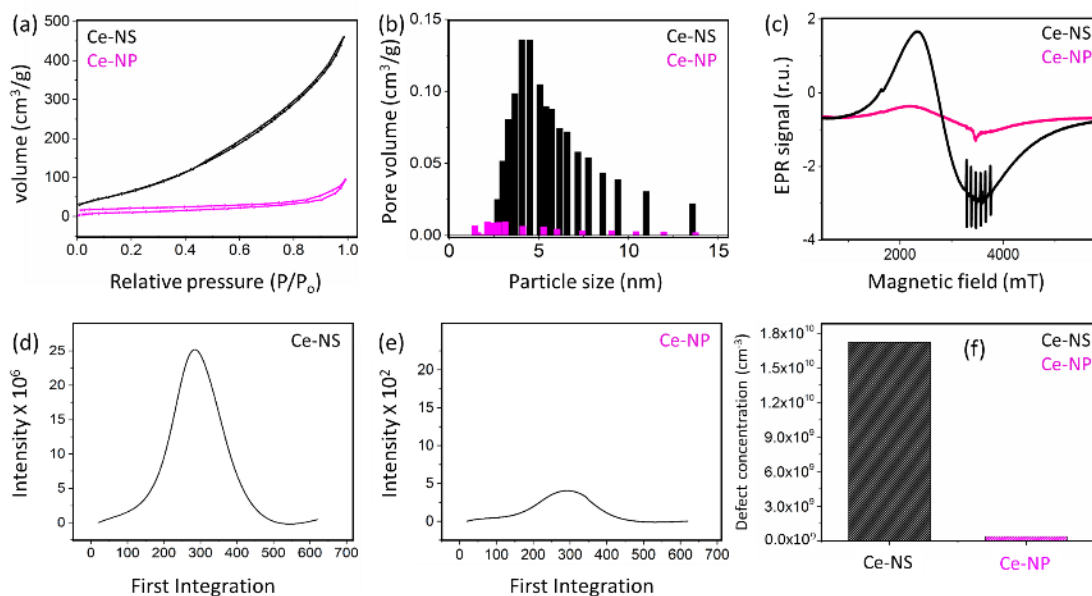


Figure S24. BET and EPR data acquired from CeO_{2-x} nanosheets (Ce-NS) and CeO_{2-x} nanoparticles (Ce-NP): (a) BET specific surface areas, (b) BET pore volume distributions, (c) EPR hyperfines showing differences in defect types, (d, e) identified maximal points applied for quantitative analysis of defects. (f) Quantified density of the total defects per cm³.

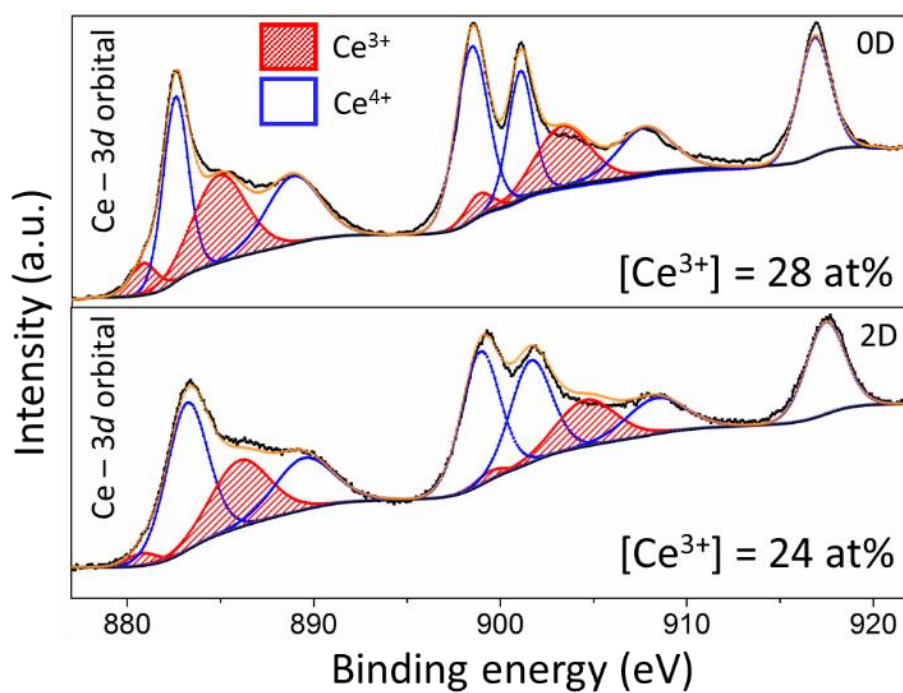


Figure S25. XPS data for 3d orbital of Ce for 0D and 2D structures.

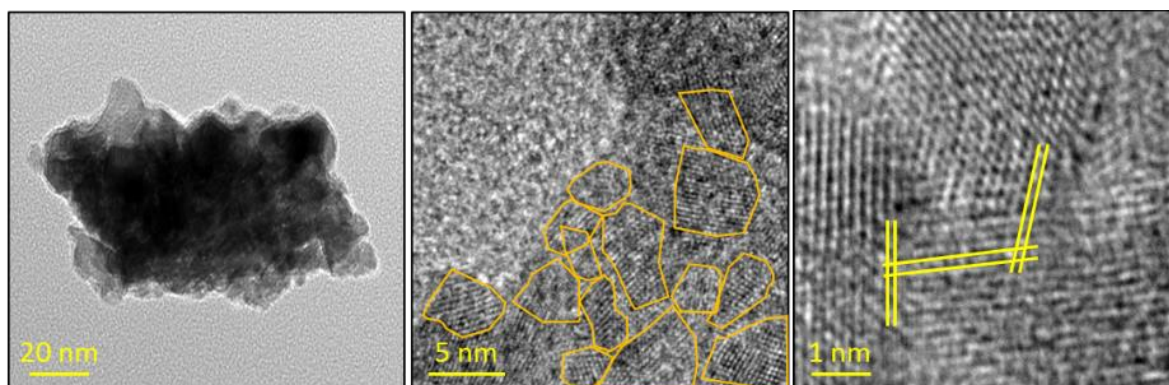


Figure S26. TEM and HRTEM images of 0D nanostructures.

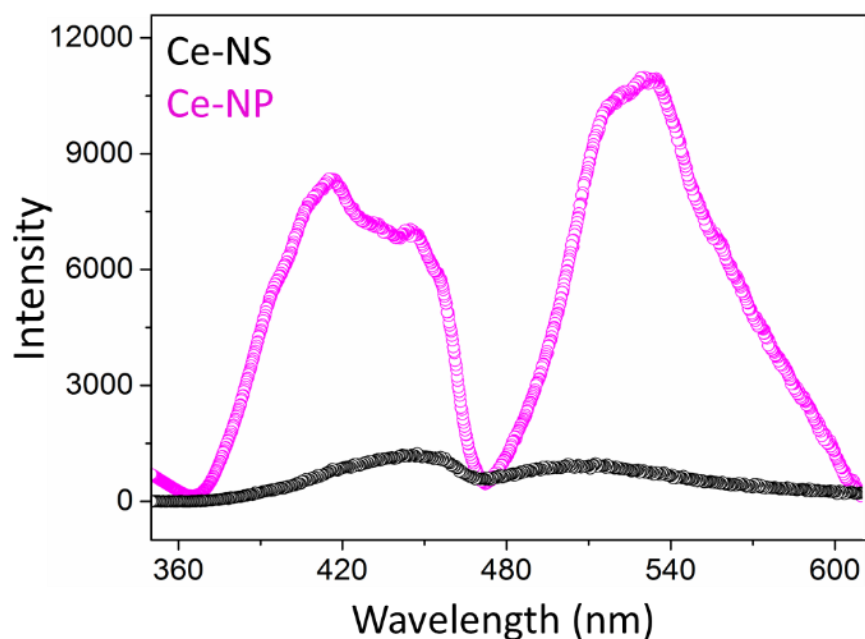


Figure S27. Photoluminescence spectra of holey 2D CeO_{2-x} (black) and CeO_2 nanoparticle (magenta).

One significant difference between 0D and 2D nanostructures is the orientation status of single crystallites in the structures. Although both nanostructures have crystallites with identical sizes (3-6 nm), the 0D structure is comprised of aggregates of single crystallites leading to the formation of large aggregated particles. However, for 2D structure, the single crystallites are strongly bonded in planar direction forming an ultrathin holey nanosheet with high density of holes across the nanosheet.

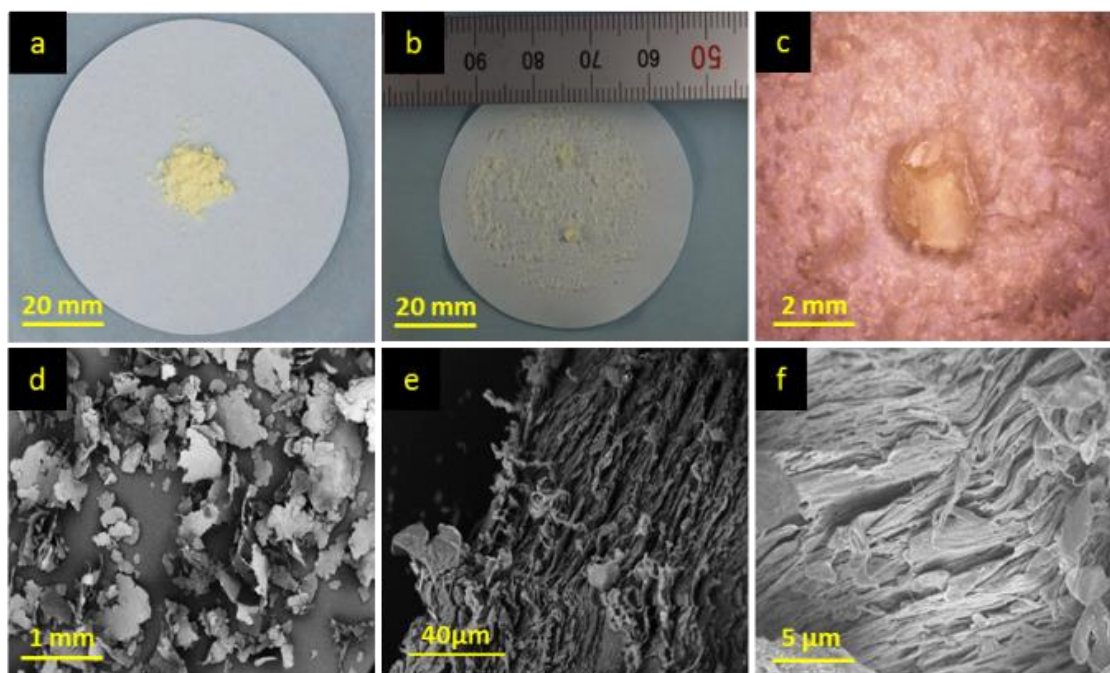


Figure S28. Large-scale synthesis of CeO_{2-x} sheets: photographs of a) Ce-CP and b) CeO_{2-x} sheets prepared by processing in water for three days. c) Optical microscope image of CeO_{2-x} sheet. d) Low magnification and e, f) high magnification SEM images of sheets stacking on top of each other, yielding a layered structure. The lateral size of some obtained sheets was ~ 5 mm.

5. Characterisation of Ti-CP, Zr-CP and derived holey metal oxide nanosheets

a) Bulk Ti-CP

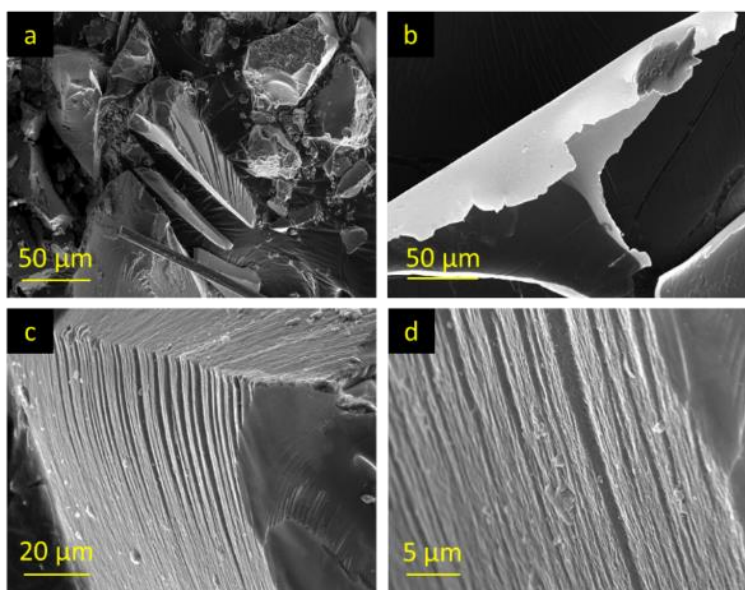


Figure S29. SEM images of Ti-CP.

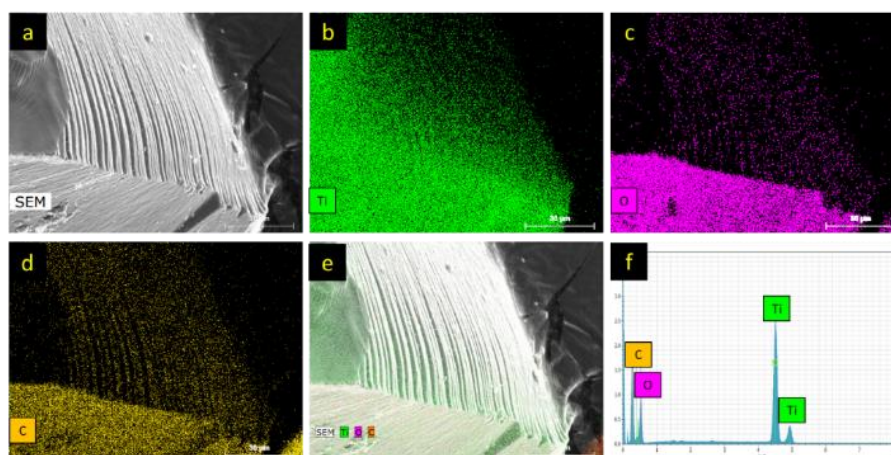


Figure S30. a) SEM image of Ti-CP. EDS elemental mapping images of b) titanium, c) oxygen and d) carbon, e) overlay of EDS images of Ti-CP and corresponding, f) EDS spectra.

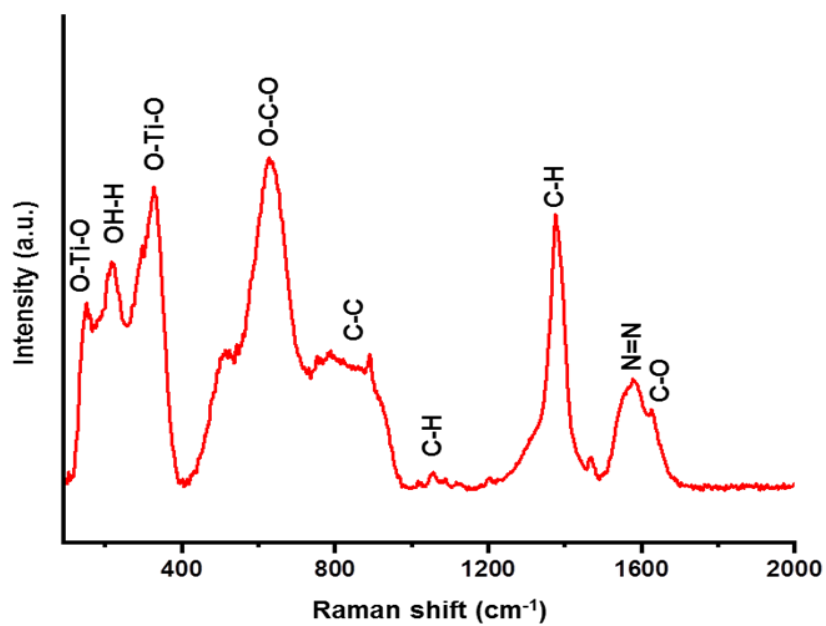


Figure S31. Raman spectra of Ti-CP.

b) Bulk Zr-CP

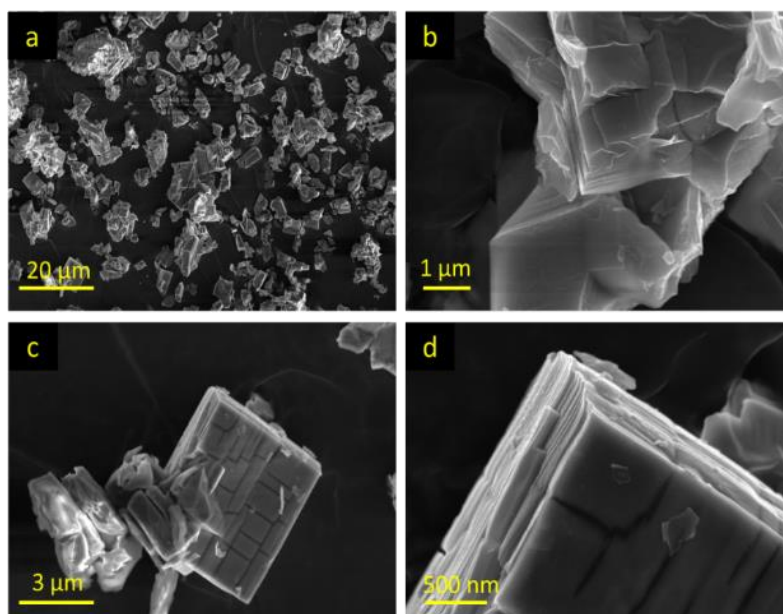


Figure S32. SEM images of Zr-CP.

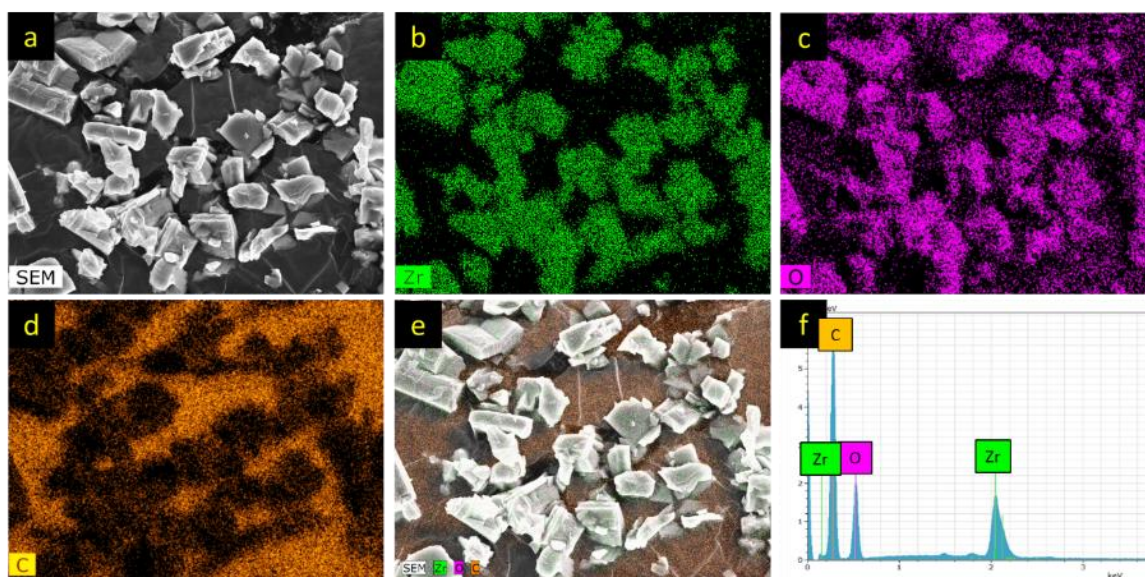


Figure S33. a) SEM image of Zr-CP, EDS elemental mapping images of b) zirconium, c) oxygen and d) carbon, e) overlay of EDS images of Zr-CP and corresponding f) EDS spectra.

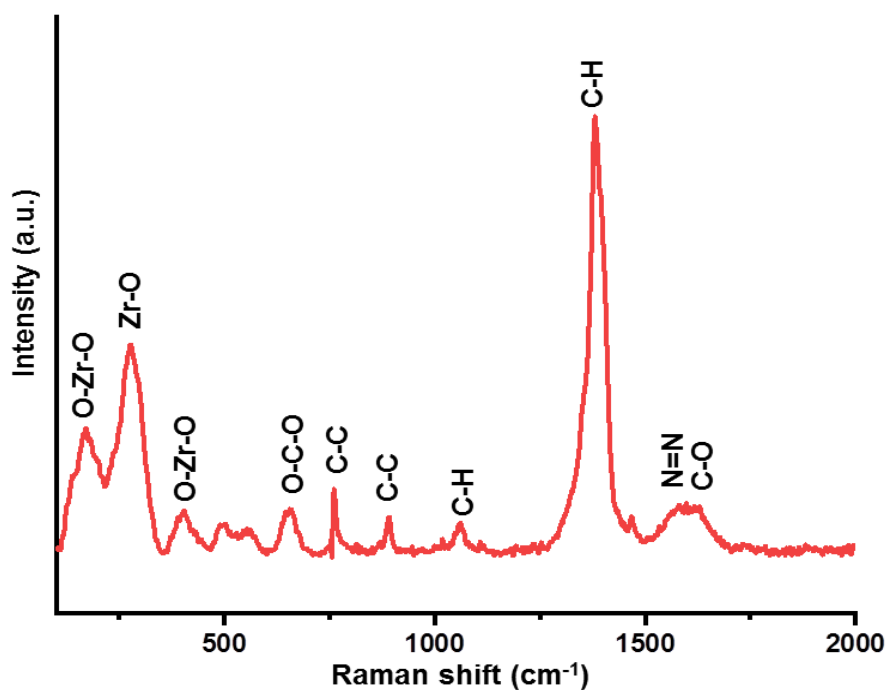


Figure S34. Raman spectra of Zr-CP.

c) Ti-CP and holey TiO₂ nanosheet

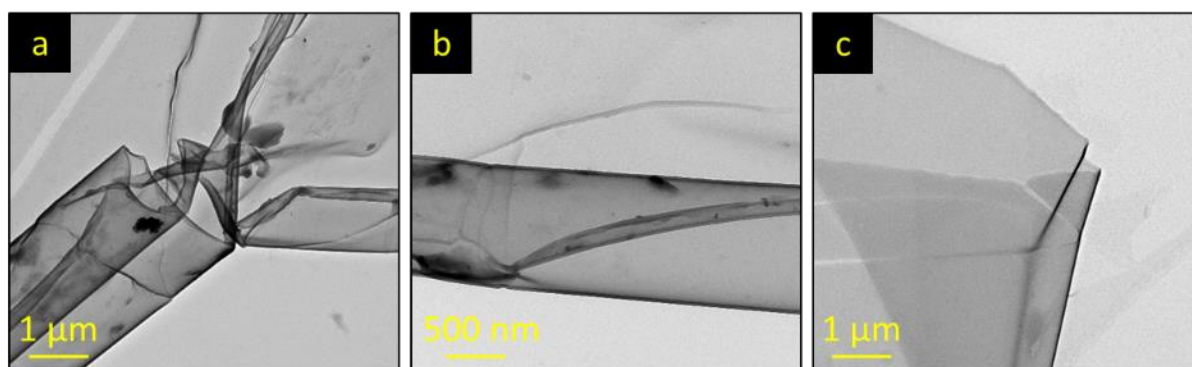


Figure S35. a-c) TEM images of ultrathin Ti-CP nanosheets exfoliating in DI water at room temperature.

Holey TiO₂ nanosheet

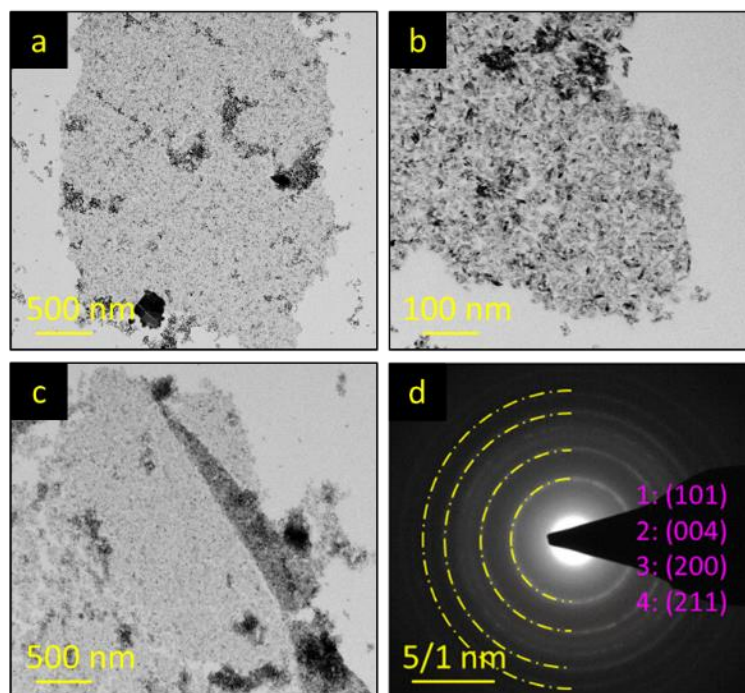


Figure S36. (a-c) TEM images of ultrathin holey TiO₂ nanosheet along with corresponding (d) SAED pattern of TiO₂ nanosheets.

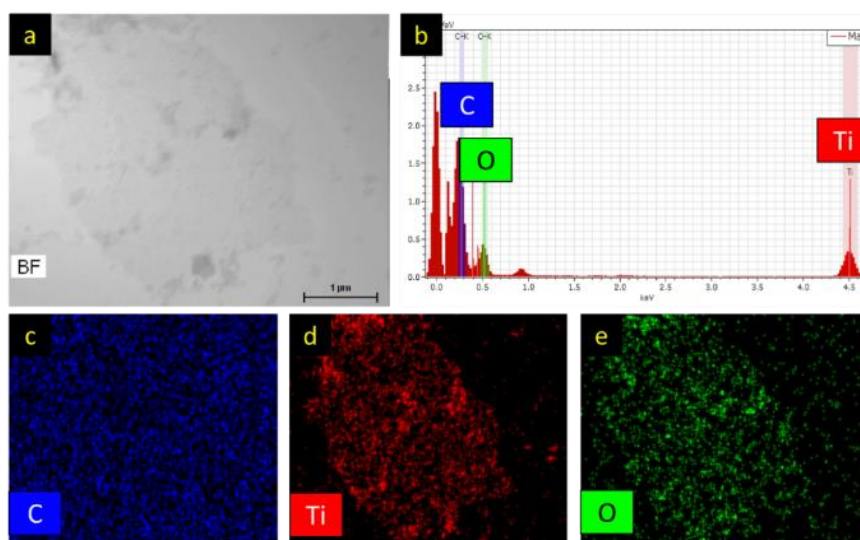


Figure S37. a) Bright field TEM image of TiO_2 (derived from Ti-CP nanosheet). b) EDS spectra and EDS elemental mapping images of c) carbon, d) titanium and e) oxygen.

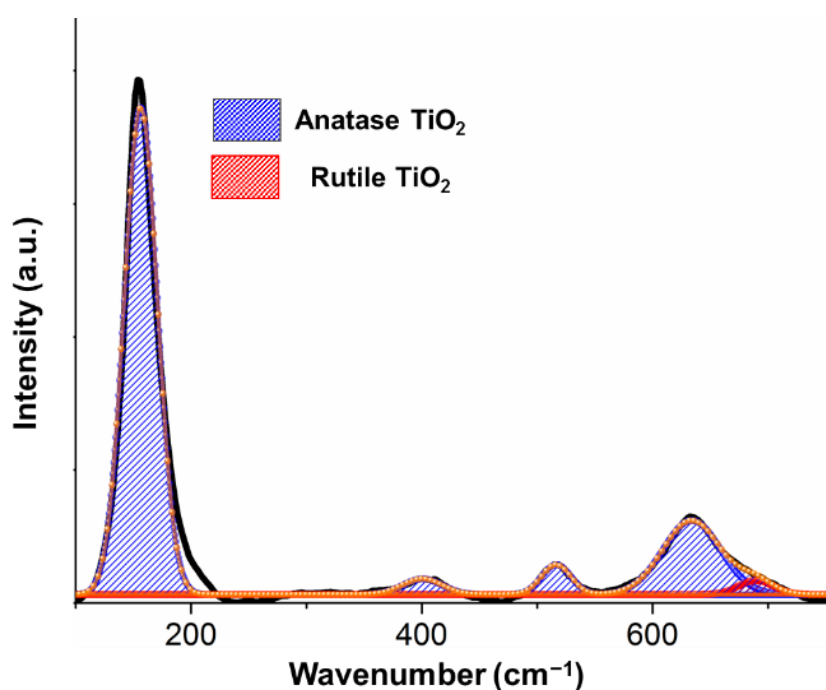


Figure S38. Raman spectrum of TiO_2 nanosheets (black) and corresponding fits for vibrational modes of anatase (blue) and rutile (red) phases.

Description of Raman data for TiO_2 nanosheet: Raman spectra collected from TiO_2 nanosheet is shown in Figure S38. According to the group theory, there are four predominant peaks attributed to TiO_2 with Raman-active modes of E_g ($\sim 144 \text{ cm}^{-1}$), B_{1g} ($\sim 397 \text{ cm}^{-1}$),

B_{1g}/A_{1g} ($\sim 516 \text{ cm}^{-1}$) and E_g ($\sim 639 \text{ cm}^{-1}$).^[26] Therefore, Raman spectra of the sample show anatase (tetragonal) TiO_2 , however slight shifts are observed in the positions of the assigned peaks. Particularly, the peak with the highest intensity is blue-shifted to 153 cm^{-1} . Similarly, the B_{1g} and E_g bands also appeared at positions different from the expected frequencies of 397 and 639 cm^{-1} , respectively. The asymmetric broadening and the observed shifts of the peaks can be explained by the phonon confinement phenomenon, which occurs by decreasing the crystal size to nano-scale.^[27] Similar Raman data have been reported for $\sim 2 \text{ nm}$ TiO_2 particles in anatase.^[28] The nanosheets in this work have a holey structure composed of nanosized crystallites with diameters of 2-4 nm (shown by the high-resolution TEM images), which can justify these slight shifts. Furthermore, a minor wide peak positioned at 690 cm^{-1} can be attributed to rutile TiO_{2-x} .

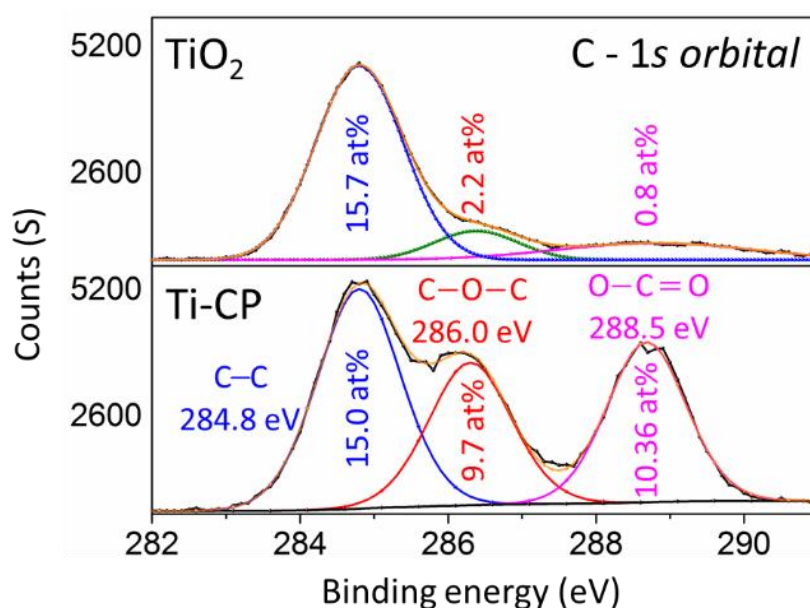


Figure S39. XPS results for 1s orbital of carbon in both Ti-CP and TiO_2 nanostructure.

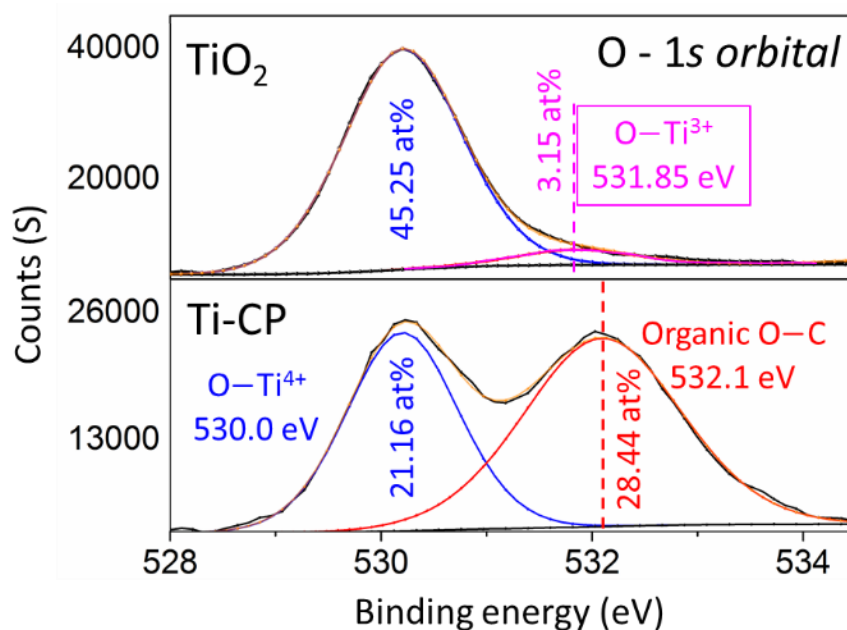


Figure S40. XPS results for 1s orbital of oxygen in both Ti-CP and TiO₂ nanostructure.

Description of XPS data: The XPS peak related to the 1s orbital of carbon for both Ti-CP and TiO₂ are shown in Figure S39. The peak positioned at 248.8 eV is attributed to the C-C bond of either the sample composition or the adsorbed contaminant on the surface of the sample.^[29] The peak positioned at 286 eV is ascribed to the C-O-C bond of formic acetate, the concentration of which is measured to be 9.70 at% by calculating the corresponding peak area. However, this amount dropped to only 2.20 at% by transformation into TiO₂ nanosheet. Further, the peak at 288.5 eV corresponds to the O-C=O bond of formic acid, the atomic percentage of which decreases by ~13 times from 10.36 at% in Ti-CP to 0.80 at% for TiO₂. The removal of formic organic linker through TiO₂ fabrication is also confirmed by investigation of the oxygen-related XPS peaks (Figure S40). The peak positioned at 532.1 eV is for 1s orbital of organic oxygen; however this peak disappeared in oxygen-related spectra of TiO₂. The two predominant peaks for 1s orbital of oxygen are O-Ti⁴⁺, and O-Ti³⁺ positioned at 530.0 eV and 531.85 eV, respectively.

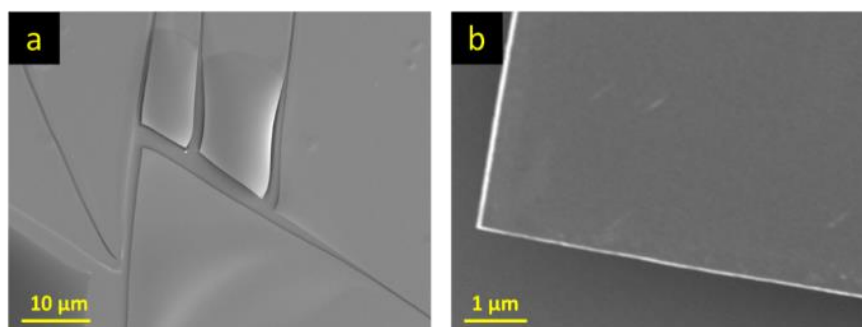
d) Zr-CP and ZrO₂ nanosheet

Figure S41. SEM images of Zr-CP nanosheets obtained by exfoliation of bulk Zr-CP in DI water.

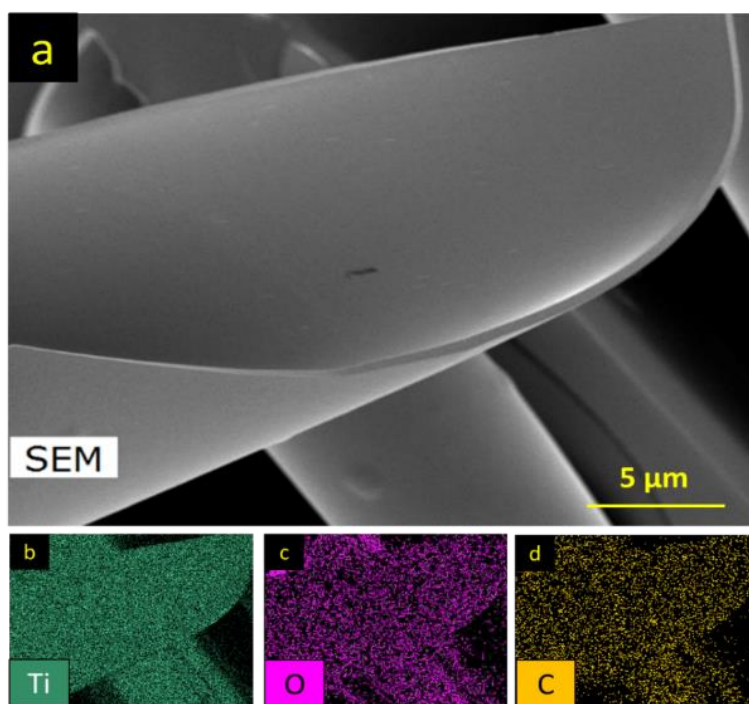


Figure S42. a) SEM image of Zr-CP nanosheets. EDS elemental mapping images of b) zirconium, c) oxygen, d) carbon.

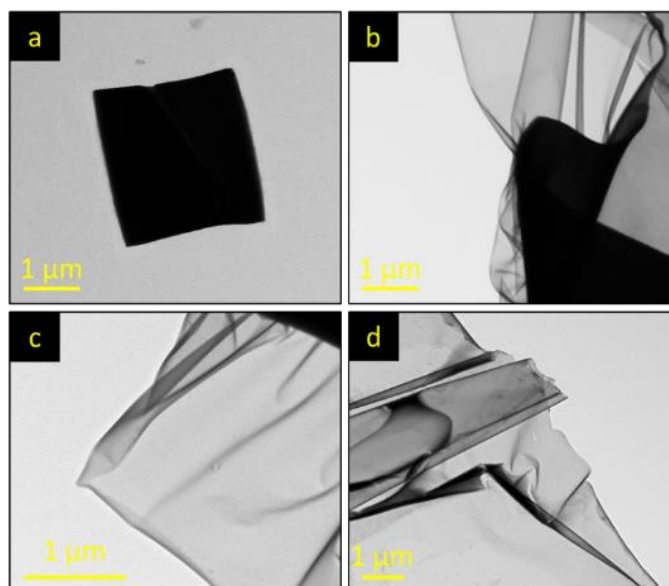


Figure S43. TEM images illustrating exfoliation of bulk Zr-CP in DI water at room temperature and formation of free-standing Zr-CP nanosheets.

ZrO₂

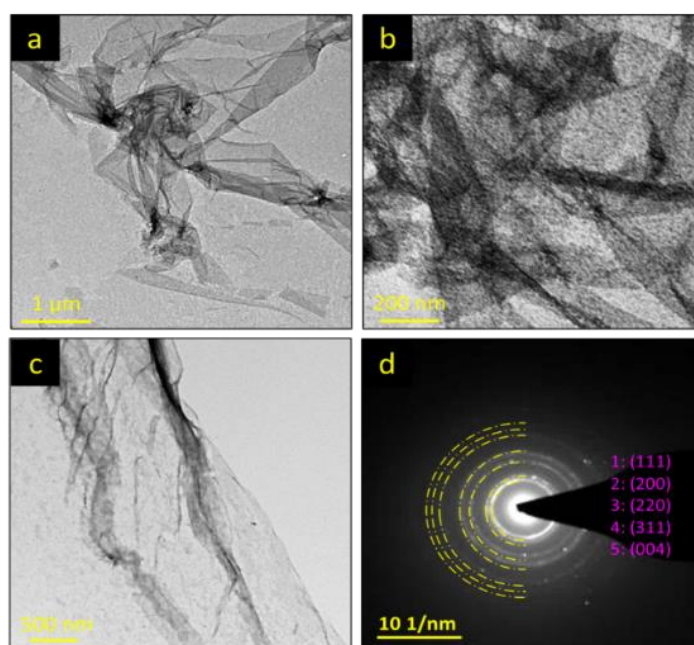


Figure S44. a-c) TEM images of ultrathin holey ZrO₂ nanosheets obtained by exfoliation of Zr-CP in DI water at room temperature. d) SAED pattern of ZrO₂ nanosheet revealing the polycrystalline nature of nanosheets.

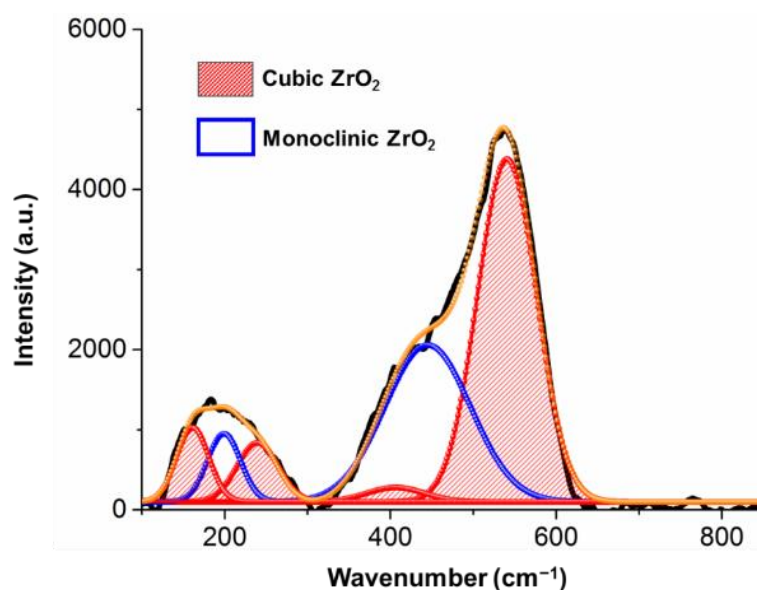


Figure S45. Raman spectrum of zirconium oxide nanosheets (black) and corresponding fits for vibrational modes of monoclinic (blue) and cubic (red) phases.

Description of Raman data for ZrO₂ nanosheet: The Raman spectra of zirconia nanosheets and the associated fits (reproduced by a set of eight Lorentzian bands corresponding to the most obvious vibrational modes) are shown in Figure S45. The bands appeared at ~195 and ~450 are attributed to the A_g vibrational modes of Zr-Zr and Zr-O for monoclinic zirconium oxide,^[30] while the broad lines consisting of two peaks at 180 and 240 cm⁻¹ as well as the most predominant peak positioned at 550 cm⁻¹, are assigned to the presence of the cubic phase.^[31] Therefore, the Raman data indicates the co-existence of the tetragonal and cubic phases in the zirconia nanosheets.

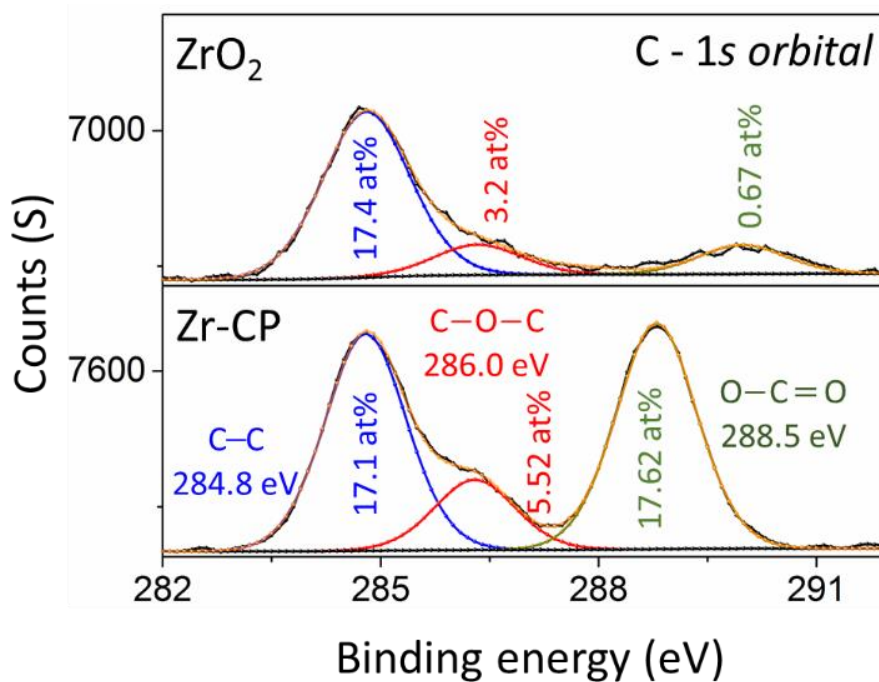


Figure S46. XPS results for 1s orbital of carbon in both Zr-CP and ZrO₂ nanostructure.

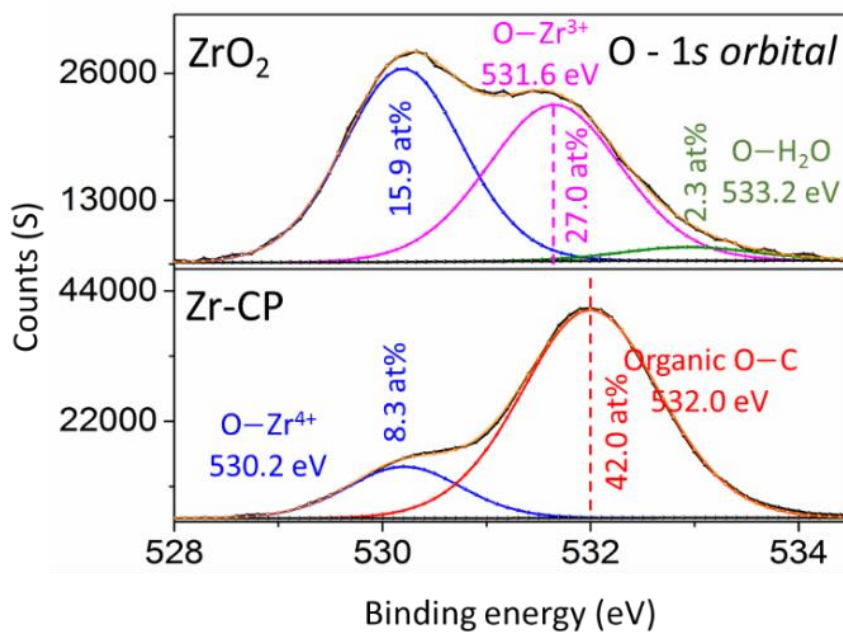


Figure S47. XPS results for 1s orbital of oxygen in both Zr-CP and ZrO₂ nanostructure.

Description of XPS data: The transformation of Zr-CP into ZrO₂ has also investigated by XPS analysis, as shown in Figure S46 and S47. The XPS peaks related to the 1s orbital of carbon for both Zr-CP (below) and ZrO₂ (top) are shown in Figure S46. The unavoidable peak positioned at 248.8 eV is attributed to the C-C bond, which mainly originates from adsorbed contaminant on the surface of the sample.^[29] The peaks at 286.0 and 288.5 eV are related to the C-O-C and O-C=O bonds of the formic acetate bonded to Zr. The total atomic percentage of these two peaks were measured to be 23.14 at% for Zr-CP that has decreased to 3.87 at% for ZrO₂. It should be noted that the peak at 286.0 eV can be attributed to the presence of CO₃ owing to the surface bonding between CO₂ of air, owing to the exposure to air, and surface oxygen of the sample and therefore, the surface bonding with CO₂ of air. This bonding is confirmed by the XPS results obtained from 1s orbital of oxygen as shown in Figure S47. The organic peak at 532.0 eV in the Zr-CP is removed in ZrO₂ related XPS spectra. Further, the small peak of Zr⁴⁺-O appearing at ~530 eV for Zr-CP has increased dramatically for ZrO₂. Interestingly, in ZrO₂, the peak at 531.6 eV, which is attributed to the O-Zr³⁺ occupies 27.0 at% of the total oxygen concentration in ZrO₂ revealing that defective ZrO₂ is formed. It should be noted that the peak positioned at 533.2 eV is related to the oxygen of adsorbed water, as reported previously.^[32]

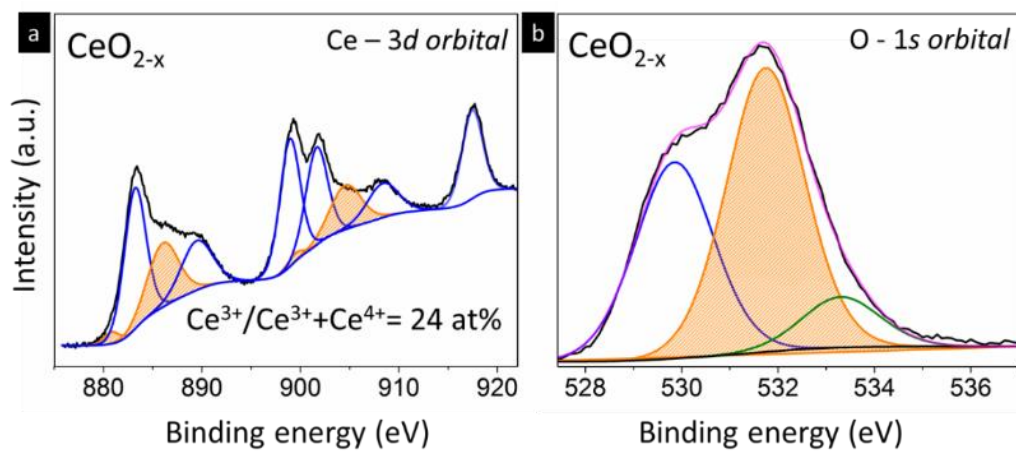


Figure S48. XPS results for $3d$ orbital of Cerium and $1s$ orbital of oxygen in CeO_{2-x} holey nanostructure.

6. Tailoring thickness and pore size of the MOs nanosheets

Table S6. Summary of nanosheet thicknesses

Metal Oxide	Crystal System	Lattice Parameter (nm)	Nanosheet Thicknesses (nm)				Number of Unit Cells			
			1.1	1.6	3.2	5.4	2	3	6	10
CeO ₂	Isotropic	0.54	1.1	1.6	3.2	5.4	2	3	6	10
TiO ₂	Anisotropic	0.60*	3.0	6.0	9.0	12.0	5	10	15	20
ZrO ₂	Isotropic	0.52	1.5	2.0	--	--	3	4	--	--

* Geometric mean of $a = 0.38$ nm and $c = 0.95$ nm is 0.60 nm

It is significant that the pH of the aqueous solution, as the dispersion medium, provides a means of controlling the porosity of the holey 2D nanosheets. To this end, the Ce-CP was dispersed in aqueous solution at the pH values of 3, 5, 7, and 9 and magnetically stirred for 8 min. The pH then was raised to 14 while stirring for an additional 15 min. The resultant 2D CeO₂ nanostructures were characterized by TEM and HRTEM imaging, as shown in Figure S49. The results show that, in highly acidic conditions (pH 3), CeO₂ forms as irregularly shaped individual nanoparticles. At pH 5, reductive solubility results in the formation of irregularly shaped pores in the range ~2 nm width x ~10 nm length. At neutral pH 7, the pores become more equiaxed and of sizes ~2-6 nm and, at pH 9, this effect becomes more pronounced, with sizes ~4-8 nm. This latter effect is explained by the Pourbaix diagram (Figure S3), which shows that increasing the pH results in conversion of Ce³⁺ to Ce⁴⁺ and that Ce³⁺-rich surfaces exhibit lower tendency to hydrate and bond with hydroxyl groups. Consequently, Ce⁴⁺-rich surfaces, with effectively homogenous OH surface functionalisation, eventually undergo

Ce(OH)₄ gelation. The rapid loss of a large volume of H₂O during the subsequent transformation to CeO₂ thus facilitates the formation of rounder and larger pores.

Further, the thickness can be controlled through the application of heating during the full period of stirring, which alters the diffusivity and hence intercalation of protons between the MCP layers. The ability to control the competing degrees of repulsion by the sheet-terminating Cl ions and the attraction by the intercalating protons provides a means of controlling the penetration of the protons and thus the thickness of the nanosheets. The outcome of this strategy is shown in the AFM images of Figure S50, which reveals MO nanosheets of decreased thicknesses by increasing the processing temperature.

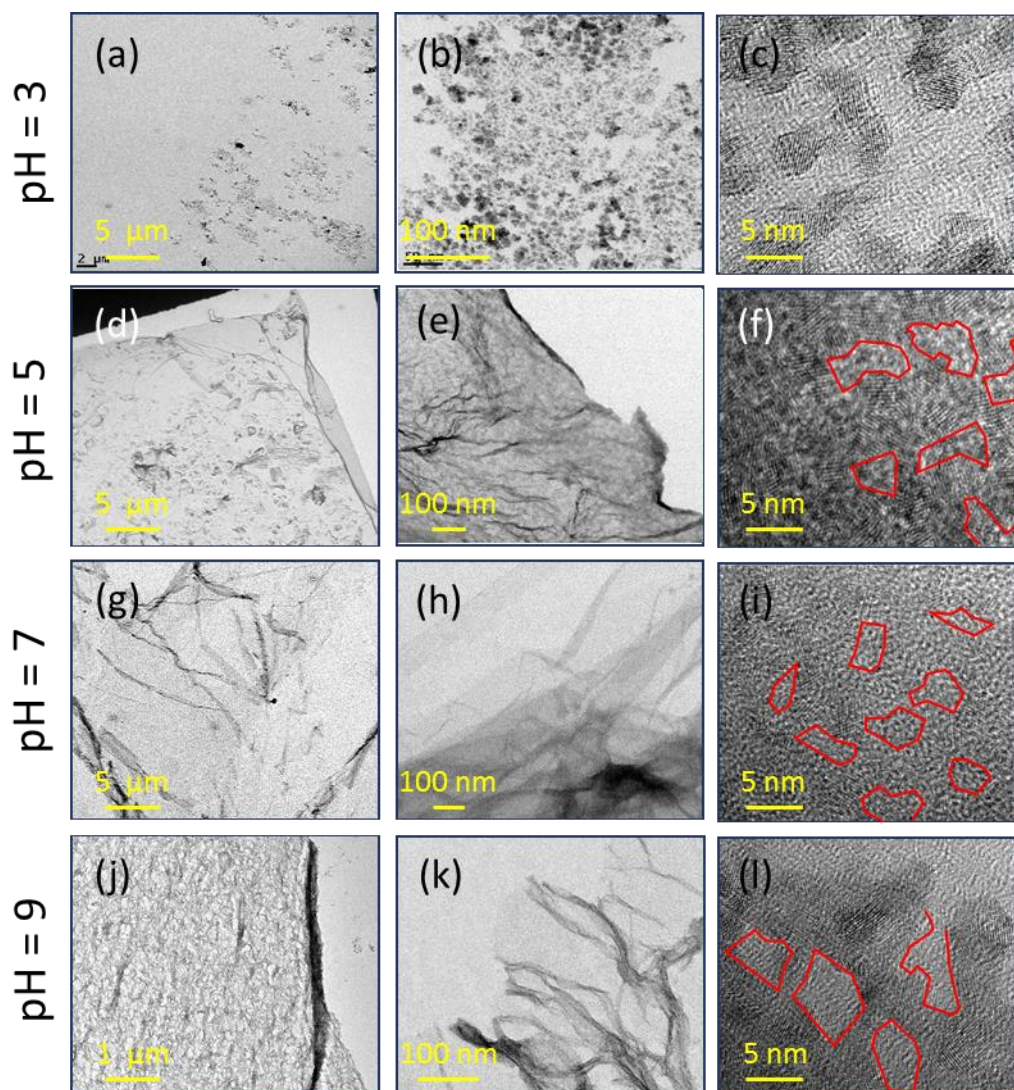


Figure S49. TEM Images of CeO_{2-x} holey nanosheets at pH 3-9

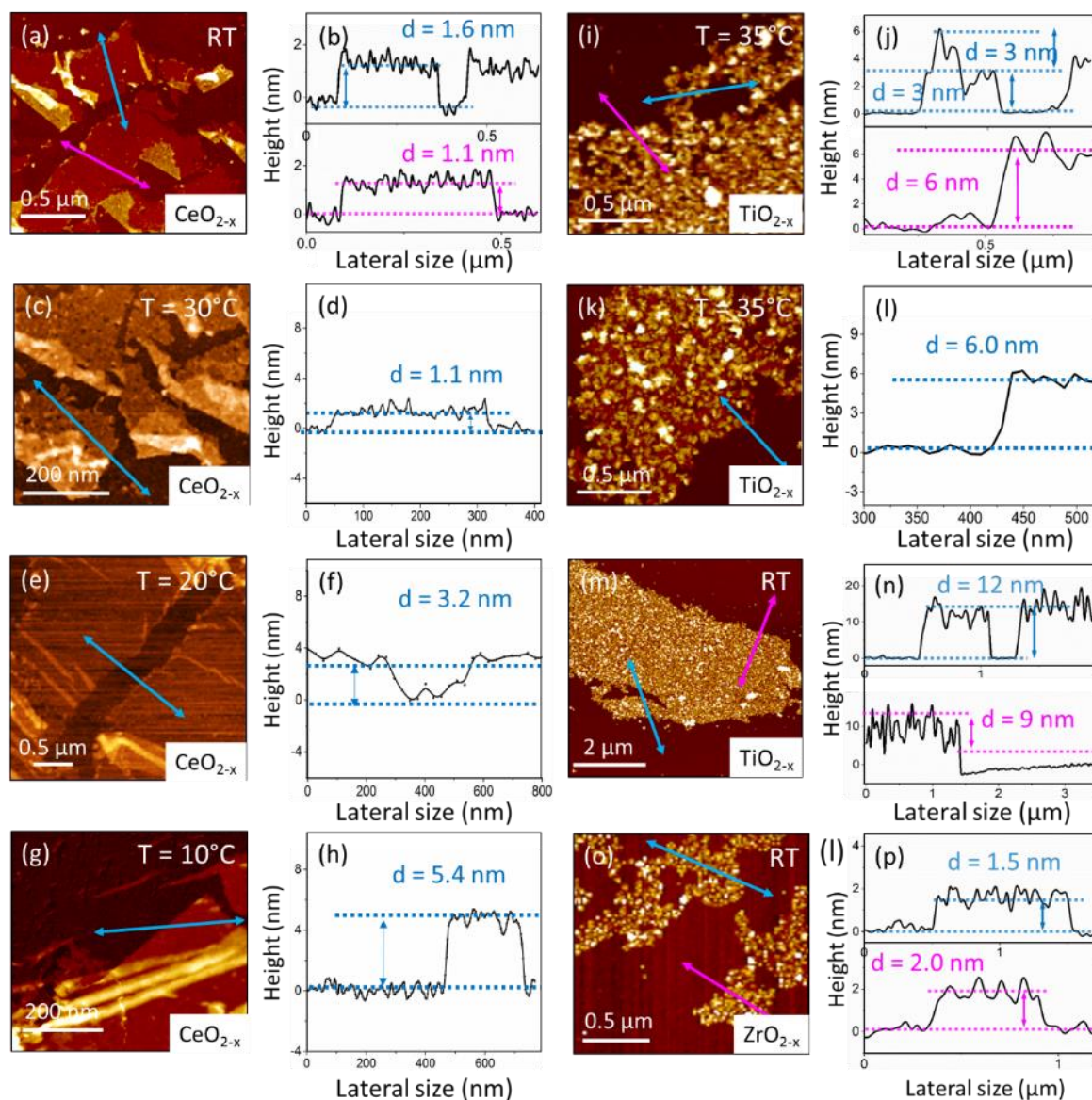


Figure S50. Thicknesses determined by AFM of nanosheets fabricated at different temperatures.

Table S7. Physical parameters of holey nanosheets

Sample	SSA ($\text{m}^2 \cdot \text{g}^{-1}$)	Pore size distribution range (nm)	Pore volume ($\text{cm}^3 \cdot \text{g}^{-1}$)
CeO_{2-x}	270	3-7	0.88
TiO_{2-x}	206	2-5	0.79
ZrO_{2-x}	76*	--	--

* Figure 3(i) confirms that discrete pores could not be detected by BET, yielding an anomalous SSA and nil pore data.

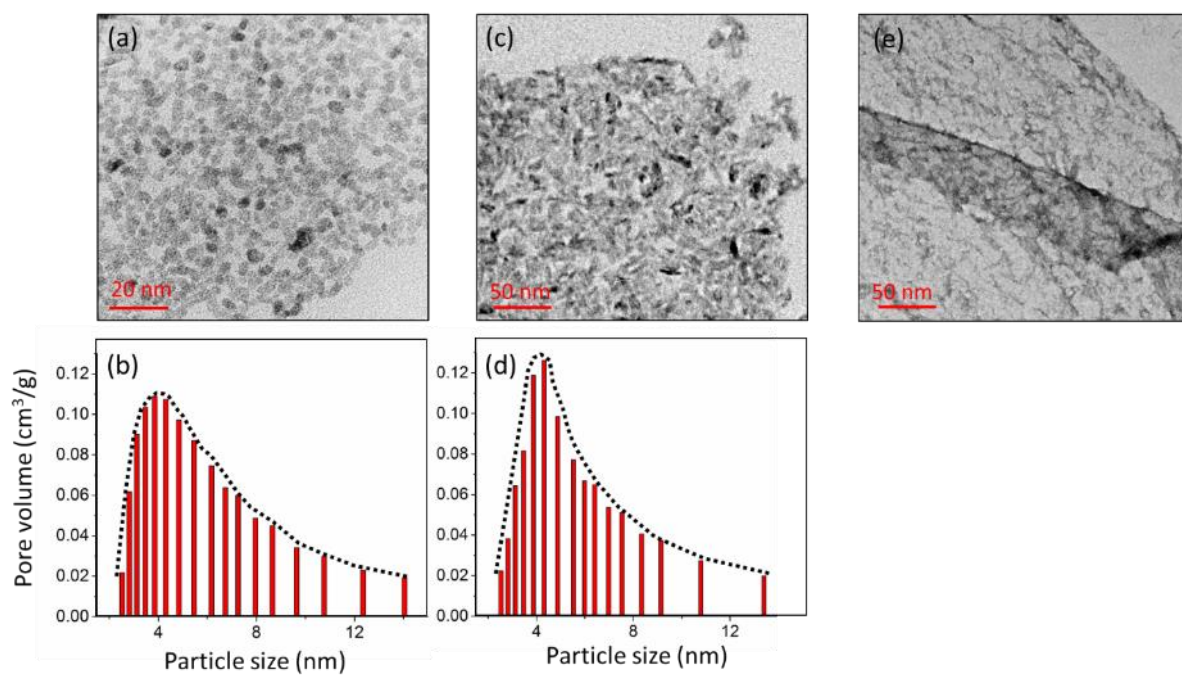


Figure S51. Size distribution analysis of the MOs. a) HRTEM image of CeO_{2-x}. b) Size distribution plot for CeO_{2-x}. c) HRTEM image of TiO_{2-x}. d) Size distribution plot for TiO_{2-x}. e) HRTEM image of ZrO_{2-x}.

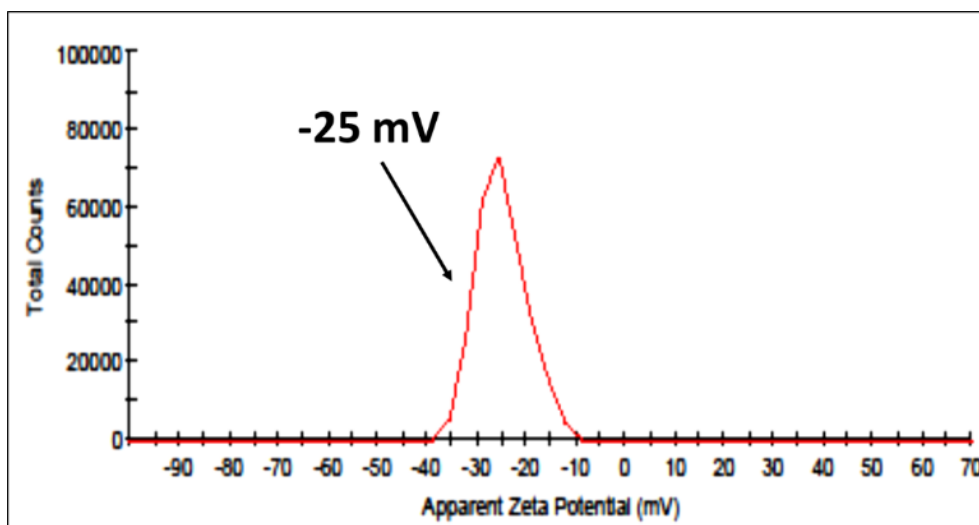
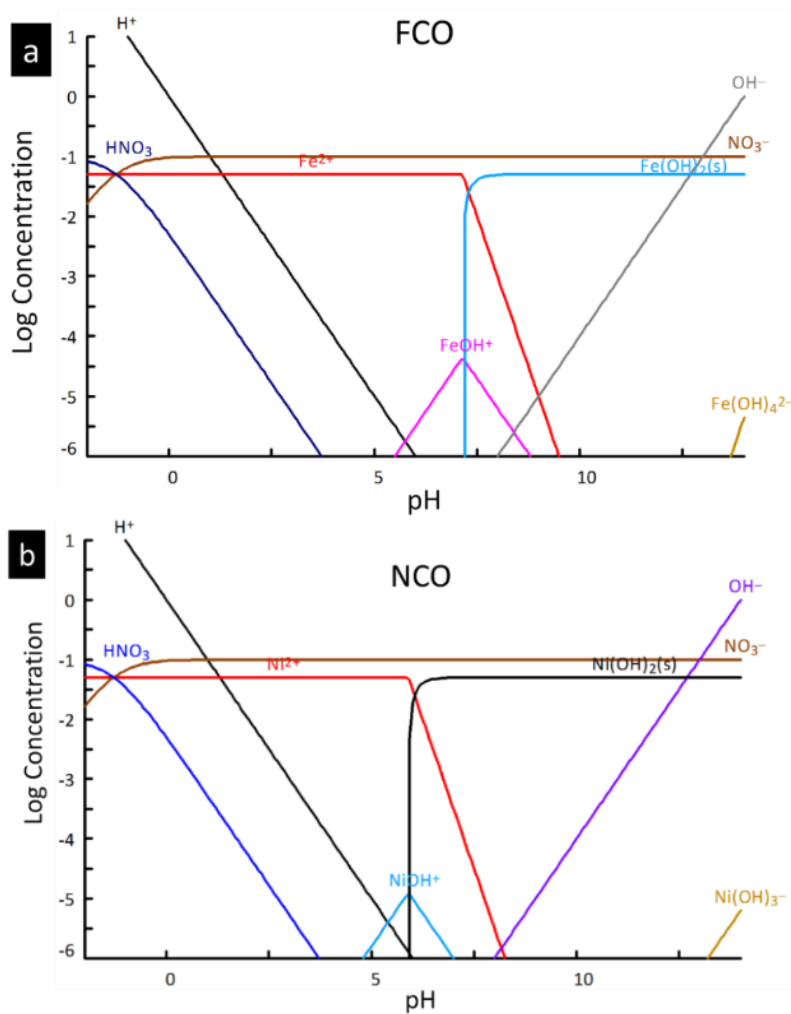
7. Characterisation of CeO_{2-x} based TMO heterojunction nanostructures

Figure S52. Zeta potentials of CeO_{2-x} in DI water.



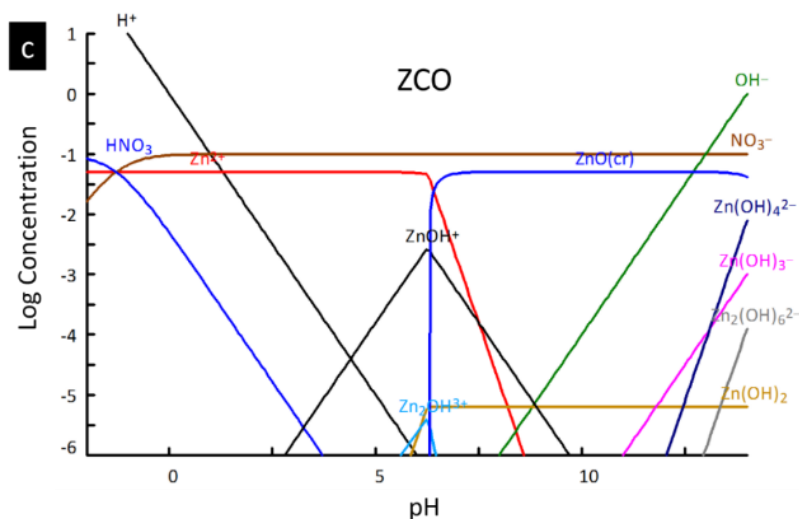


Figure S53. Speciation diagrams for a) Fe (II), b) Ni (II), c) Zn (II) species representing stability of the species and concentration variations of species as a function of pH in aqueous solution.

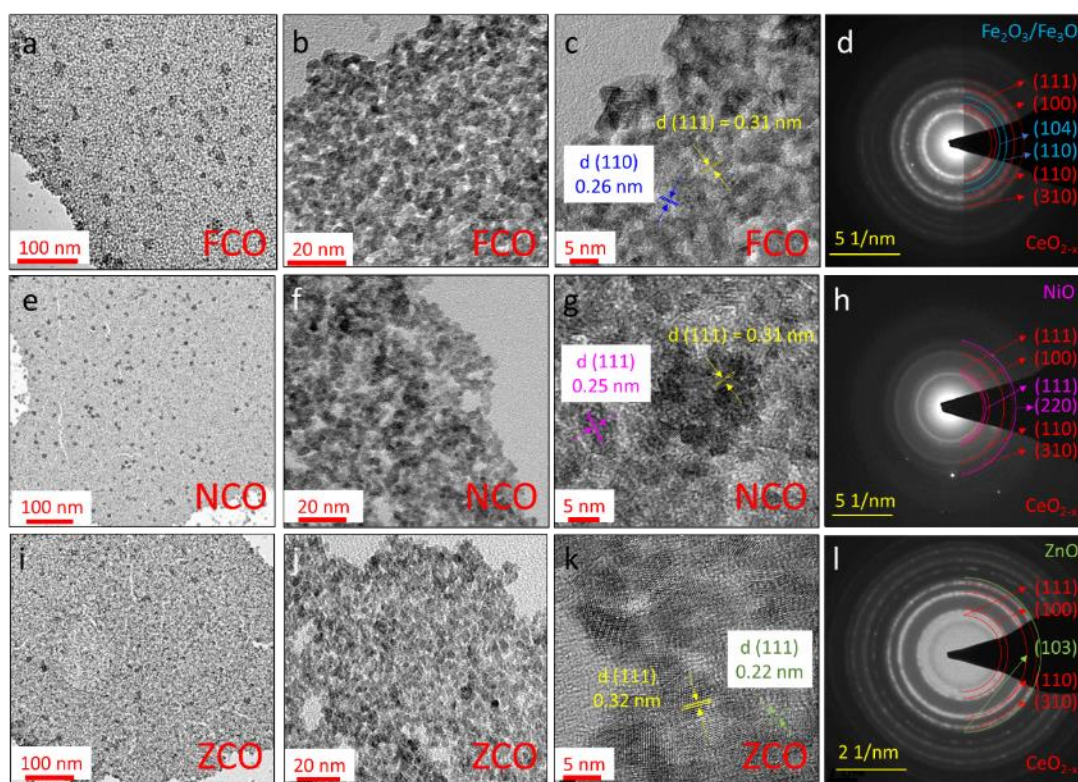


Figure S54. a-c) TEM and HRTEM image of FCO; d) SAED pattern of FCO. e-g) TEM and HRTEM image of NCO. h) SAED pattern of NCO. i-k) TEM and HRTEM image of ZCO. l) SAED pattern of ZCO.

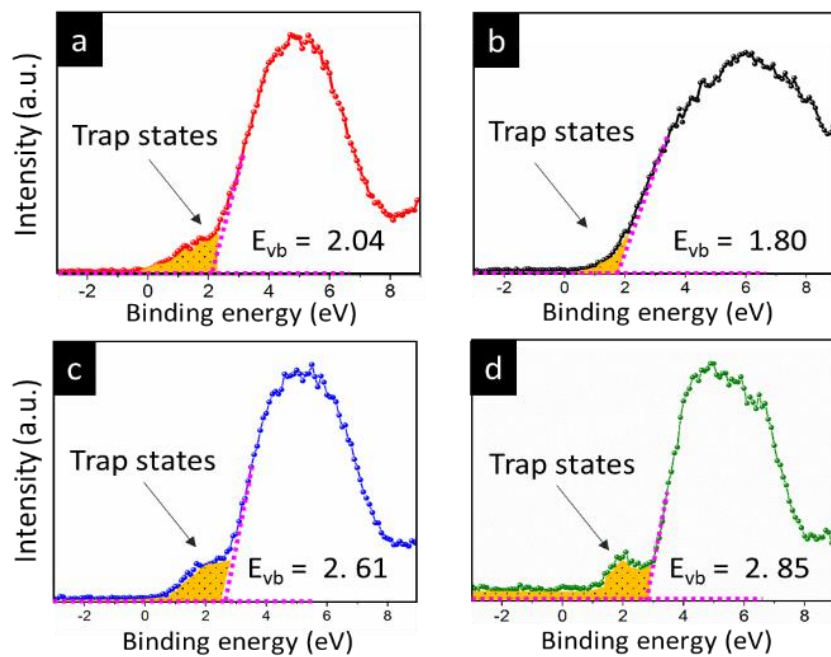


Figure S55. XPS valence measurement of a) holey CeO_{2-x} nanosheet, b) FCO, c) NCO, and d) ZCO.

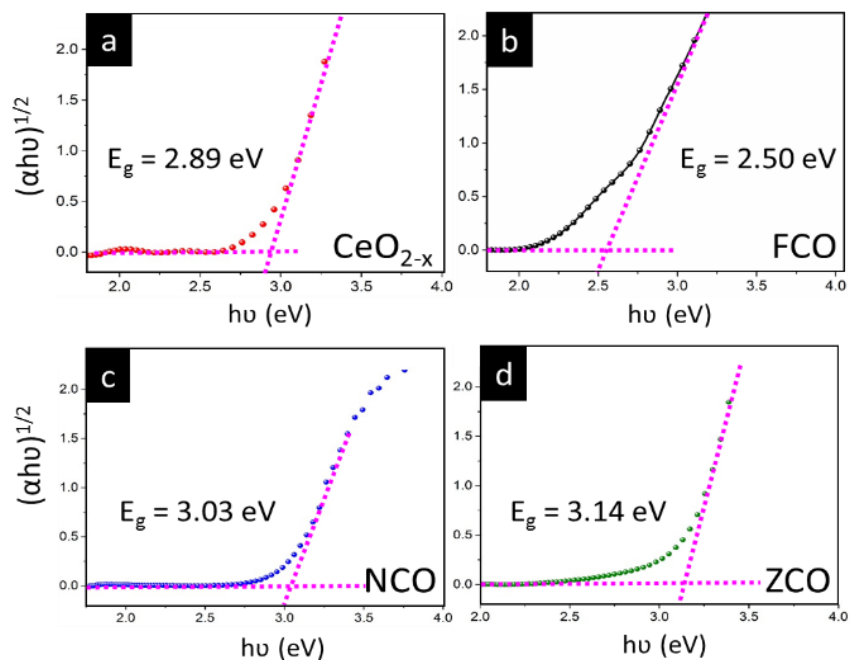


Figure S56. Tauc plot for a) holey CeO_{2-x} nanosheet, b) FCO, c) NCO, and d) ZCO.

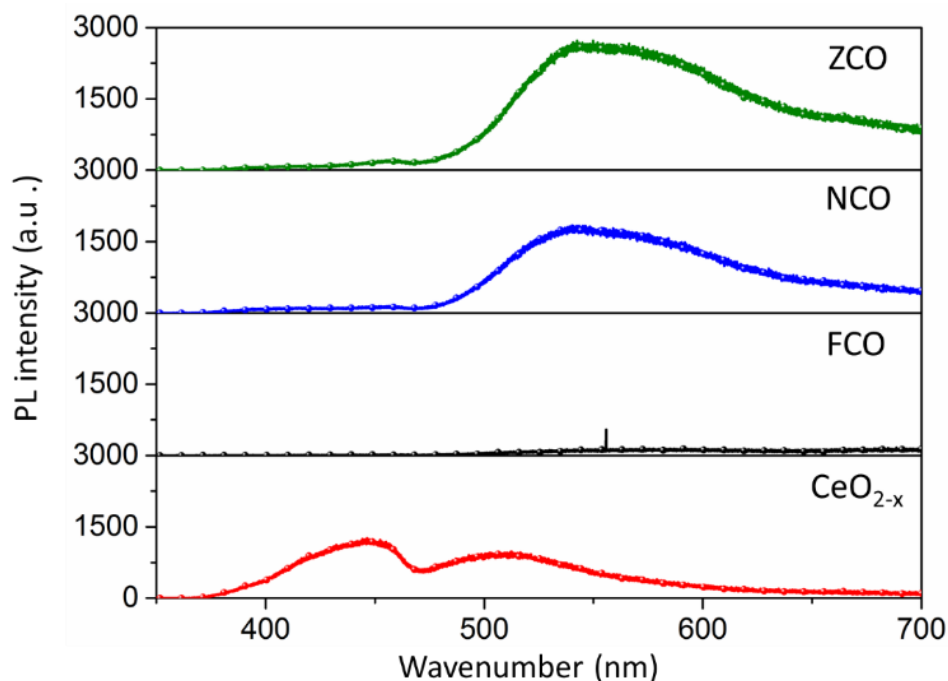


Figure S57. Photoluminescence spectra of CeO_{2-x} (red), FCO (black), NCO (blue), ZCO (green).

The room temperature photoluminescence (PL) emission of the CeO_{2-x} and the heterojunction structures are shown in Figure S57. The PL spectra for CeO_{2-x} nanosheet show two small and broad emissions with a wavelength of 426 nm (blue emissions) and 510 (green emissions). The former is attributed to the $\text{F}^{++} \rightarrow 4f_1$ transition, as the F^{++} state is just below the $4f_0$ band acting as an electron trap and $4f_1$ state acts as a hole trap.^[33] However, the latter, originates from the presence of Ce^{3+} , as a hole trap state, and oxygen vacancy, as an electron trapping state. The radiative recombination of these two traps lead to the excitation at the wavelength of 510 nm. The low PL intensity of these two emissions for CeO_{2-x} nanosheet, compared to the reported CeO_2 nanostructures, again confirms the short diffusion pathways for charge carriers and hence reduction of radiative recombination.

As for FCO, the intensity of the peaks decrease towards zero, indicating minimal electron/hole recombination, owing to the rapid charge carrier separations through very short diffusion routes. The broad emission band positioned at ~ 450 nm originates from the surface oxygen

vacancies,^[34] confirming the high concentration of oxygen vacancies in atomically thin CeO_{2-x} holey nanosheet. Adding NiO and ZnO resulted in a considerable reduction of near band edge UV emission peaks while the shift towards the deep-level (DL) emissions within green wavenumber. This reduction can be attributed to the sp-d exchange interactions between the band electrons of the localized d electrons of the Ni^{2+} and Zn^{2+} and CeO_{2-x} nanosheet.^[35] Further, the high intensity of the DL emission shows increasing defect concentrations in both NCO and ZCO. The increase in the defect concentration is also confirmed by determining the trapping sites from XPS valence band results (Figure S55). As for NiO, The green emission band at 560 nm is attributed to the defects in the NiO lattice, *e.g.*, Schottky pair defects, interstitial oxygen trapping, and nickel vacancies produced by charge transfer between Ni^{2+} and Ni^{3+} ions.^[34] For ZCO, the small and broad emission peaks positioned at 390 nm is attributed to the recombination of the free excitons through an exciton-exciton collision process,^[36] which is insignificant for all the heterojunction nanostructures. The weak and broad blue emission band at ~460 nm is a deep level emission (DLE) originating from the oxygen vacancies or interstitial zinc ions of ZnO nanomaterials. A broad green emission band was observed at 550 nm for all ZnO nanomaterials which may be ascribed to the existence of defects such as singly ionized oxygen vacancies.^[36-37]

8. Photocatalytic activities of CeO_{2-x} based TMO heterojunction structures

The photocatalytic performance of the samples was assessed by degradation analysis of methylene blue (MB) compound, which is used extensively for photocatalytic analysis,^[14] under solar light irradiation. The gradual decrease of intensity of the absorbance peak of MB, which is centred at 664 cm⁻¹, in the presence of the nanosheets was measured. Figure S58a shows the absorption spectra corresponding to the mixed nanosheet and MB solution as a function of irradiation time. The considerable reduction of the absorption peak in the first 40 min is an indication of rapid chemical breakdown of MB followed by almost diminishing of the peak after 2 h. The kinetics of the photodegradation were explored by plotting $\ln(A_t/A_0)$, where A_t is the dye absorption at time (t) and A_0 is the dye absorbance prior to irradiation, against irradiation time using a pseudo first-order reaction model,^[38] as shown in Figure S58b. Additionally, Figure S58c illustrates a plot comparing the dye degradation performance of the holey nanosheets synthesised in this work and a selection of best previously-reported performances. The experimental conditions of the work are summarized in Table S8. Further, FCO, with a visible light region bandgap, exhibits a remarkable enhancement in dye degradation performance by almost 100% degradation after 2 h (Figure S58d).

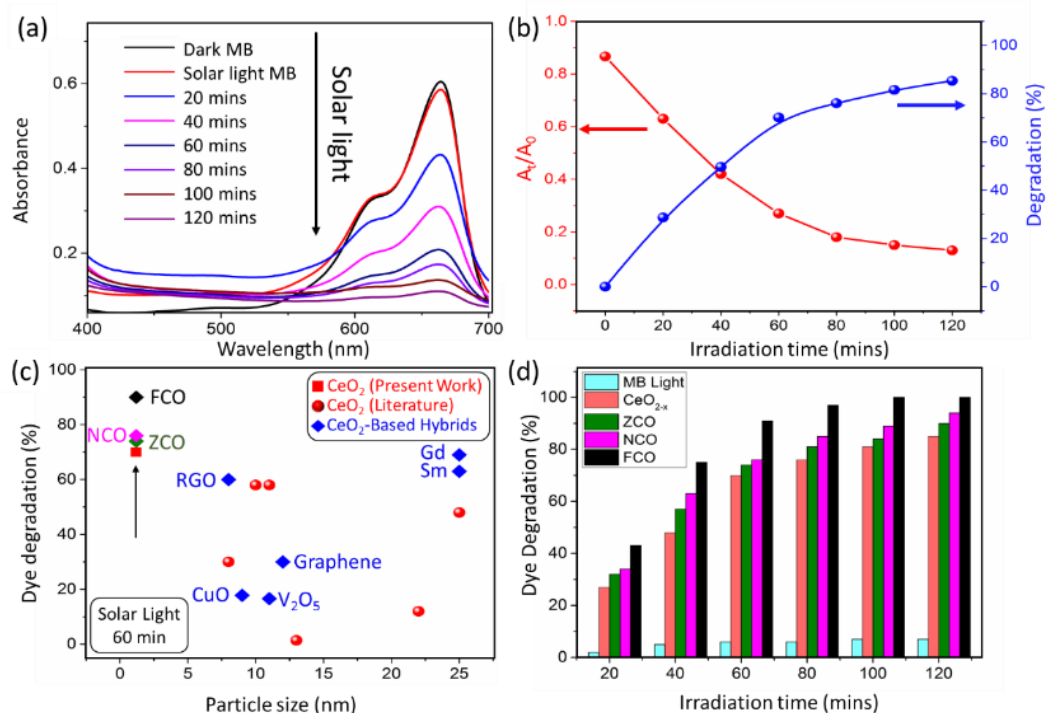


Figure S58 a) MB degradation in the presence of holey nanosheet (blue bar) and NiO (purple) and Fe_2O_3 (green) anchored holey nanosheet. b) The kinetics of the MB degradation. c) Performance stability study on the holey nanosheet after 5 degradation tests. d) Summary of MB degradation performances of CeO_{2-x} structures.

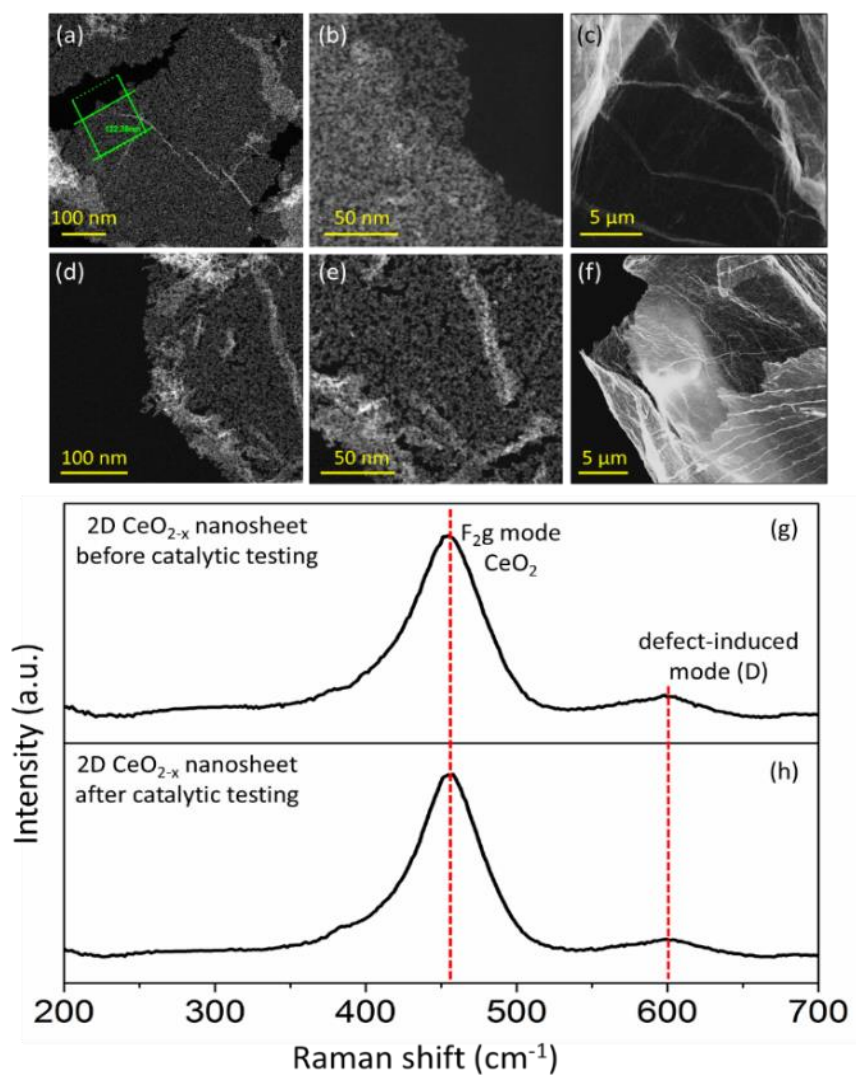


Figure S59 CeO_2 nanosheet before and after catalytic testing (solar light irradiation): (a, b) dark field TEM images before testing, (c) SEM image before testing, (d, e) dark field TEM images after testing, (f) SEM image after testing, (g) Raman pattern before testing, (h) Raman pattern after testing.

Table of Comparison

The outstanding performance of the nanosheets can be attributed to two mechanisms: 1) High density of structural defects modifying the electronic properties of the nanosheets by narrowing the bandgap. The atomic layer of the nanosheet offers a high surface-to-volume ratio, which considerably enhances the exposed facets at the dye-nanosheet interfacial region. Such novel

architecture is reported for the first time for CeO₂ structures. 2) This performance is shown to be improved significantly by fabrication of mixed heterojunction nanostructures that minimize the density of electron/hole recombination, introduces a high number of defects which act as active sites, thereby resulting in high numbers of ROS within the solution to catalyse the dye degradation.

Table S8. Comparison of photocatalytic activity (methylene blue degradation) of different nanostructures of CeO₂ and CeO₂-based materials.

Material	Morphology	Dimensions (nm)	Dye concentration (mol L ⁻¹)	Solids Loading (mg mL ⁻¹)	Light Source	Degradation for 1 h (%)	Ref.
CeO ₂	Particle	8	5 x 10 ⁻⁷	1	Sunlight	~30	[39]
RGO-CeO ₂	NS-Particle	8	5 x 10 ⁻⁷	1	Solar light	~60	[39]
CeO ₂ -CuO	irregular	9	1.5 x 10 ⁻⁵	1	Sunlight	17.8	[40]
CeO ₂ -V2O5	Irregular	11	1.5 x 10 ⁻⁵	1	Sunlight	16.6	[40]
CeO ₂	irregular	13	1.5 x 10 ⁻⁵	1	Sunlight	1.4	[40]
CeO ₂ -RGO	spherical	~12	0.37 x 10 ⁻⁶	0.8	Visible light	30	[41]
CeO _{2-x}	octahedron	~22	0.60 x 10 ⁻⁶	0.1	Visible light	12	[42]
CeO ₂	Irregular	11	0.5 x 10 ⁻⁵	2	Solar light	60	[43]
CeO ₂	Hollow sphere	10000	2.5 x 10 ⁻⁵	0.52	Solar light	60	[44]
CeO ₂	Irregular	~25	N/A	N/A	Solar light	~48	[45]
Gd-CeO ₂	Irregular	~17	N/A	N/A	Solar light	~27	[45]
Sm-CeO ₂	Irregular	~18	N/A	N/A	Solar light	~33	[45]
CeO _{2-x}	Holey 2D	~1	1 x 10 ⁻⁵	0.5	Solar light	~70	This Work
FCO	Holey 2D	~1	1 x 10 ⁻⁵	0.5	Solar light	~90	This Work
NCO	Holey 2D	~1	1 x 10 ⁻⁵	0.5	Solar light	~76	This Work
ZCO	Holey 2D	~1	1 x 10 ⁻⁵	0.5	Solar light	~74	This Work

As shown in Table S9, the agglomerated 0D/0D nanostructures exhibit lower surface areas compared to those of the 0D/2D nanostructures. The lower photocatalytic performances of the former are attributed mainly to the high electron/hole recombination rate and lower accessible surface area, as suggested by the PL data of Figure S27 and S57.

Table S9. Comparative data for physical properties and photocatalytic performances of 0D/0D and 0D/2D structures.

Sample	Dimensionality	CeO ₂ Crystallite Size (nm)	BET Specific Surface Area (m ² g ⁻¹)	Photodegradation after 1 h (%)	Ref.
CeO ₂	0D	3-6	51	23.0	This work
CeO ₂	2D	3-6	270	70.0	
Fe-CeO ₂	0D/0D	3-6	58	26.0	
Fe-CeO ₂	0D/2D	3-6	267	90.0	
Fe-CeO ₂	0D/0D	6-8	101	31.8	
Ni-CeO ₂	0D/2D	3-6	-	76.0	
Zn-CeO ₂	0D/0D	4-10	39	24.2	
Zn-CeO ₂	0D/2D	3-6	-	74.0	
Cu-CeO ₂	0D/0D	3-6	118	50.0	
Cu-CeO ₂	0D/0D	9	-	17.8	
Zn-CeO ₂	0D/0D	9	26	5.5	46
Zn-CeO ₂	0D/0D	6	13	28.0	46
V-CeO ₂	0D/0D	11	-	16.6	40
Gd-CeO ₂	0D/0D	17	-	27.0	45
Sm-CeO ₂	0D/0D	18	-	33.0	45

9. References

- [1] a) O. S. Khalipova, V. Lair, A. Ringuedé, *Electrochim. Acta* **2014**, *116*, 183; b) V. Lair, L. S. Živković, O. Lupan, A. Ringuedé, *Electrochim. Acta* **2011**, *56*, 4638-4644.
- [2] W. Liang, R. Babarao, M. J. Murphy, D. M. D'Alessandro, *Dalton Trans.* **2015**, *44*, 1516.
- [3] G. Kresse, D. Joubert, *Phys. Rev. B* **1999**, *59*, 1758.
- [4] a) J. P. Perdew, K. Burke, M. Ernzerhof, *Phys. Rev. Lett.* **1996**, *77*, 3865; b) J. P. Perdew, K. Burke, M. Ernzerhof, *Phys. Rev. Lett.* **1997**, *78*, 1396.
- [5] G. Kresse, J. Furthmüller, *Comput. Mater. Sci.* **1996**, *6*, 15.
- [6] a) M. Dion, H. Rydberg, E. Schröder, D. C. Langreth, B. I. Lundqvist, *Phys. Rev. Lett.* **2004**, *92*, 246401; b) J. Klimeš, D. R. Bowler, A. Michaelides, *Phys. Rev. B* **2011**, *83*, 195131.
- [7] C. Cazorla, J. Boronat, *Rev. Mod. Phys.* **2017**, *89*, 035003.
- [8] J. P. Perdew, A. Ruzsinszky, G. I. Csonka, O. A. Vydrov, G. E. Scuseria, L. A. Constantin, X. Zhou, K. Burke, *Phys. Rev. Lett.* **2008**, *100*, 136406.
- [9] G. Kresse, J. Furthmüller, *Phys. Rev. B* **1996**, *54*, 11169.
- [10] S. L. Dudarev, G. A. Botton, S. Y. Savrasov, C. J. Humphreys, A. P. Sutton, *Phys. Rev. B* **1998**, *57*, 1505.
- [11] P. E. Blöchl, *Phys. Rev. B* **1994**, *50*, 17953.
- [12] A. V. Krukau, O. A. Vydrov, A. F. Izmaylov, G. E. Scuseria, *J. Chem. Phys.* **2006**, *125*, 224106.
- [13] G. Henkelman, A. Arnaldsson, H. Jónsson, *Comput. Mater. Sci.* **2006**, *36*, 354.
- [14] a) C. Boerigter, R. Campana, M. Morabito, S. Linic, *Nat. Commun.* **2016**, *7*, 10545; b) Y.-C. Chen, Y.-K. Hsu, R. Popescu, D. Gerthsen, Y.-G. Lin, C. Feldmann, *Nat. Commun.* **2018**, *9*, 232; c) W. Wang, N. Xie, L. He, Y. Yin, *Nat. Commun.* **2014**, *5*, 5459; d) Z. Lian, M. Sakamoto, H. Matsunaga, J. J. M. Vequizo, A. Yamakata, M. Haruta, H. Kurata, W. Ota, T. Sato, T. Teranishi, *Nat. Commun.* **2018**, *9*, 2314; e) L. Weng, H. Zhang, A. O. Govorov, M. Ouyang, *Nat. Commun.* **2014**, *5*, 4792.
- [15] D. Channei, S. Phanichphant, A. Nakaruk, S. Mofarah, P. Koshy, C. Sorrell, *Catalysts* **2017**, *7*, 45.
- [16] N. Kanagathara, N. G. Renganathan, M. K. Marchewka, N. Sivakumar, K. Gayathri, P. Krishnan, S. Gunasekaran, G. Anbalagan, *Spectrochim. Acta A-Molecular and Biomolecular Spectroscopy* **2013**, *101*, 112.
- [17] E. Spinner, *J. Chem. Soc. (Resumed)* **1964**, 4217.
- [18] D. A. Long, *J. Raman Spectrosc.* **2004**, *35*, 905.
- [19] a) A. C. Cabral, L. S. Cavalcante, R. C. Deus, E. Longo, A. Z. Simões, F. Moura, *Ceram. Int.* **2014**, *40*, 4445; b) *J. Raman Spectrosc.* **1992**, *23*, 267.
- [20] V. N. Krishnamurthy, S. Soundararajan, *J. Less Common Met.* **1967**, *13*, 263.
- [21] C. Barth, C. Laffon, R. Olbrich, A. Ranguis, P. Parent, M. Reichling, *Sci. Rep.* **2016**, *6*, 21165.
- [22] J. Rodríguez-Carvajal, *Phys. B-Condensed Matter* **1993**, *192*, 55.
- [23] M. H. N. Assadi, V. Sahajwalla, *Chem. Phys.* **2014**, *443*, 107.
- [24] a) S. Maintz, V. L. Deringer, A. L. Tchougréeff, R. Dronskowski, *J. Comput. Chem.* **2013**, *34*, 2557; b) S. Maintz, V. L. Deringer, A. L. Tchougréeff, R. Dronskowski, *J. Comput. Chem.* **2016**, *37*, 1030.
- [25] A. J. Locock, in *Structural Chem. Inorg. Actinide Comp.* (Eds.: S. V. Krivovichev, P. C. Burns, I. G. Tananaev), Elsevier, Amsterdam, **2007**, pp. 217.
- [26] T. Ohsaka, F. Izumi, Y. Fujiki, *J. Raman Spectrosc.* **1978**, *7*, 321.
- [27] A. K. Arora, M. Rajalakshmi, T. R. Ravindran, V. Sivasubramanian, *J. Raman Spectrosc.* **2007**, *38*, 604.
- [28] K.-R. Zhu, M.-S. Zhang, Q. Chen, Z. Yin, *Phys. Lett. A* **2005**, *340*, 220.
- [29] W.-F. Chen, P. Koshy, C. C. Sorrell, *J. Mater. Sci.* **2016**, *51*, 2465.
- [30] M. ISHIGAME, T. SAKURAI, *J. Am. Ceram. Soc.* **1977**, *60*, 367.

- [31] a) F. Davar, A. Hassankhani, M. R. Loghman-Estarki, *Ceram. Int.* **2013**, *39*, 2933; b) M. N. Tahir, L. Gorgishvili, J. Li, T. Gorelik, U. Kolb, L. Nasdala, W. Tremel, *Solid State Sci.* **2007**, *9*, 1105.
- [32] R. Mehmood, S. S. Mofarah, W. F. Chen, P. Koshy, C. C. Sorrell, *Inorg. Chem.* **2019**, *58*, 6016.
- [33] K. S. Hemalatha, K. Rukmani, *RSC Adv.* **2016**, *6*, 74354.
- [34] B. Karthikeyan, T. Pandiyarajan, S. Hariharan, M. S. Ollakkan, *CrystEngComm* **2016**, *18*, 601.
- [35] J. K. Salem, T. M. Hammad, R. R. Harrison, *J. Mater. Sci.: Mater. Electron.* **2012**, *24*, 1670.
- [36] L. Saikia, D. Bhuyan, M. Saikia, B. Malakar, D. K. Dutta, P. Sengupta, *App. Catal. A: General* **2015**, *490*, 42.
- [37] R. Sakthivel, A. Shankar Ganesh, A. Geetha, B. Anandh, R. Kannusamy, K. Tamilselvan, *Orient. J. Chem.* **2017**, *33*, 355.
- [38] a) N. Syed, A. Zavabeti, M. Mohiuddin, B. Zhang, Y. Wang, R. S. Datta, P. Atkin, B. J. Carey, C. Tan, J. van Embden, A. S. R. Chesman, J. Z. Ou, T. Daeneke, K. Kalantar-zadeh, *Adv. Funct. Mater.* **2017**, *27*, 1702295; b) R. S. Datta, J. Z. Ou, M. Mohiuddin, B. J. Carey, B. Y. Zhang, H. Khan, N. Syed, A. Zavabeti, F. Haque, T. Daeneke, K. Kalantar-zadeh, *Nano Energy* **2018**, *49*, 237.
- [39] S. Kumar, A. Kumar, *Mater. Sci. Eng., B* **2017**, *223*, 98.
- [40] R. Saravanan, S. Joicy, V. K. Gupta, V. Narayanan, A. Stephen, *Mater. Sci. Eng. C, Mater.* **2013**, *33*, 4725.
- [41] M. E. Khan, M. M. Khan, M. H. Cho, *Sci. Rep.* **2017**, *7*, 5928.
- [42] M. M. Khan, S. A. Ansari, D. Pradhan, D. H. Han, J. Lee, M. H. Cho, *Ind. Eng. Chem. Res.* **2014**, *53*, 9754.
- [43] V. Ramasamy, V. Mohana, V. Rajendran, *OpenNano* **2018**, *3*, 38-47.
- [44] J. Qian, Z. Chen, C. Liu, X. Lu, F. Wang, M. Wang, *Mater. Sci. Semicon. Proc.* **2014**, *25*, 27.
- [45] M. K. Chinnu, P. Anandan, M. Arivanandhan, A. Venkatesan, R. M. Kumar, R. Jayavel, *J. Mater. Sci.: Mater. Electron.* **2018**, *29*, 9564.
- [46] S. Rajendran, M. M. Khan, F. Gracia, J. Qin, V. K. Gupta, S. Arumainathan, *Sci. Rep.* **2016**, *6*, 31641.